The Astrophysical Journal Supplement Series, 214:16 (19pp), 2014 October doi:10.1088/0067-0049/214/2/16

THREE-DIMENSIONAL BOLTZMANN HYDRO CODE FOR CORE COLLAPSE IN MASSIVE STARS. I. SPECIAL RELATIVISTIC TREATMENTS

Hiroki Nagakura[1], Kohsuke Sumiyoshi[2], and Shoichi Yamada[3,4]
[1] Yukawa Institute for Theoretical Physics, Kyoto University, Oiwake-cho, Kitashirakawa, Sakyo-ku, Kyoto 606-8502, Japan
[2] Numazu College of Technology, Ooka 3600, Numazu, Shizuoka 410-8501, Japan
[3] Advanced Research Institute for Science & Engineering, Waseda University, 3-4-1 Okubo, Shinjuku, Tokyo 169-8555, Japan
[4] Department of Science and Engineering, Waseda University, 3-4-1 Okubo, Shinjuku, Tokyo 169-8555, Japan
Received 2014 July 20; accepted 2014 August 8; published 2014 September 18

ABSTRACT

We propose a novel numerical method for solving multi-dimensional, special relativistic Boltzmann equations for neutrinos coupled with hydrodynamics equations. This method is meant to be applied to simulations of core-collapse supernovae. We handle special relativity in a non-conventional way, taking account of all orders of v/c. Consistent treatment of the advection and collision terms in the Boltzmann equations has been a challenge, which we overcome by employing two different energy grids: *Lagrangian remapped* and *laboratory fixed* grids. We conduct a series of basic tests and perform a one-dimensional simulation of core-collapse, bounce, and shock-stall for a 15 $M_{\odot}$ progenitor model with a minimum but essential set of microphysics. We demonstrate in the latter simulation that our new code is capable of handling all phases in core-collapse supernova. For comparison, a non-relativistic simulation is also conducted with the same code, and we show that they produce qualitatively wrong results in neutrino transfer. Finally, we discuss a possible incorporation of general relativistic effects into our method.

Key words: hydrodynamics – neutrinos – supernovae: general

Online-only material: color figures

1. INTRODUCTION

Quantitative studies on the mechanism of core-collapse supernovae (CCSNe) require detailed numerical simulations. Except for low-mass (8–10 $M_{\odot}$) progenitors, elaborate one-dimensional (1D) simulations under spherical symmetry have not reproduced the supernova explosion (Sumiyoshi et al. 2005; Liebendörfer et al. 2005; Kitaura et al. 2006; Burrows et al. 2007). In the past decade, most of the supernova modelers have focused on the multi-dimensional (multi-D) aspects of dynamics (see, e.g., Kotake et al. 2012b; Janka 2012; Burrows 2013 for recent reviews). In the post-bounce phase, instabilities drive post-shock accretion flows into turbulence, making dynamics intrinsically multi-D. This may be crucial for supernova explosions, since the non-spherical turbulent motions increase the time for material to dwell in the gain region, enhancing its absorption of hot neutrinos, boosting the post-shock pressure, and eventually pushing the shock wave outward (Takiwaki et al. 2012; Dolence et al. 2013).

As a matter of fact, we have recently witnessed shock revival in some of the currently most advanced simulations (Burrows et al. 2006; Marek & Janka 2009; Suwa et al. 2010; Lentz et al. 2012; Müller et al. 2012a, 2012b; Takiwaki et al. 2014), which has raised our hope that we will finally uncover the mechanism behind CCSNe. Unfortunately, however, success or failure of the supernova explosion is a delicate problem. In fact, the latest results of multi-D simulations by different groups are still at odds with one another and no consensus has yet emerged concerning which ingredient(s) is (are) essential for explosion. Although various approaches, both phenomenological and ab initio, are being undertaken at present, only better simulations, possibly ones with a Boltzmann equation solver, that incorporate detailed microphysics and general relativity (GR) may give a conclusive answer.

To achieve this goal, we are developing a numerical code for neutrino transfer, which solves the Boltzmann equations (Sumiyoshi & Yamada 2012). Our code is based on the discrete-ordinate S_n method, which determines the finite differences of the Boltzmann equations, deploying multi-angle and multi-energy bins in momentum space. Using some snapshots from three-dimensional (3D) supernova simulations, Sumiyoshi & Yamada (2012) demonstrated the capabilities of this new code, which implements the minimum set of neutrino reactions (see also Sumiyoshi et al. 2014). These simulations concerned neutrino transfer in static backgrounds, however, and no back-reactions to matter were taken into account.

The next step should be a coupling of this code with a hydrodynamical one, however, this method may not be so simple. Spherically symmetric 1D computations may be easier, since they can adopt Lagrangian formulations for both neutrino transfer and hydrodynamics (Mezzacappa & Bruenn 1993; Mezzacappa et al. 2001; Liebendörfer et al. 2005; Sumiyoshi et al. 2005, 2007). Formalisms such as these could not be applied in multi-D, however, and different formulations should be developed for the multi-D Boltzmann hydro simulations, i.e., simulations that solve the Boltzmann equations and hydrodynamical equations simultaneously in multiple dimensions.

Unlike the previous 1D codes, we adopt an Eulerian picture in this paper. There are several reasons for making this choice. Among other things, we have in mind that the Boltzmann solver will be coupled with multi-D Eulerian hydrodynamics and gravity solvers, which have been well established and widely used in the high-energy astrophysical community. In addition, the Eulerian picture has the benefit of easily handling the left-hand side of the Boltzmann equation, i.e., the advection terms. In general, Lagrangian formulations need to treat derivatives with respect to neutrino energy, which correspond to the Doppler effect caused by spatial and/or temporal variations in fluid velocities. This may cause problems particularly at a shock wave, where fluid velocities are discontinuous. For these reasons, we have opted for the Eulerian approach.

It should be noted, however, that the Eulerian approach has its own demerits. For example, we normally need to handle transformations between the laboratory frame and the fluid restframe

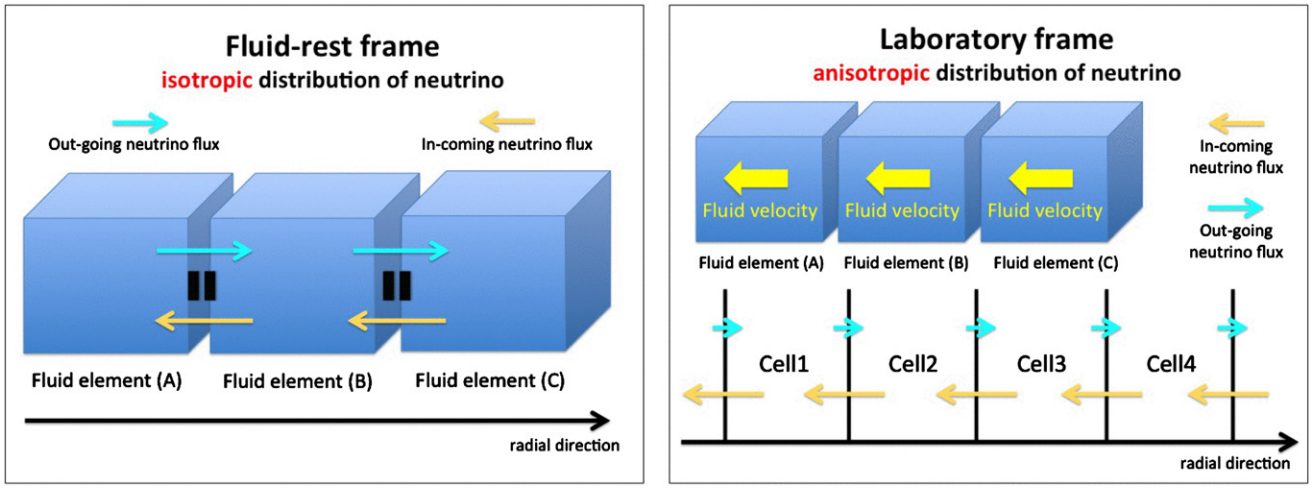

Figure 1. Left panel: incoming and outgoing neutrino fluxes at the interface between fluid elements, which are measured on the fluid restframe. Right panel: the neutrino fluxes are displayed in the laboratory frame, in which matter is moving inward. The bottom picture shows that the incoming (yellow) fluxes are larger than the outgoing (blue) ones at the interfaces of laboratory-fixed spatial grids.

(A color version of this figure is available in the online journal.)

defined locally, which are nothing but Lorentz transformations for flat spacetime, since neutrino–matter interactions are best described in the fluid restframe. Physically consistent treatments of both advection and collision terms in the multi-D Boltzmann solver are technically difficult particularly in the S_n method, since special relativistic (SR) effects such as Doppler shifts and aberrations should be handled on a rather coarse grid in the momentum space (see Section 3 for more details). Previous studies have attempted to alleviate this difficulty by employing an expansion of basic equations up to $\mathcal{O}(v/c)$ (see, e.g., Hubeny & Burrows 2007). In CCSNe, the maximum fluid velocity is around 10% of the speed of light and such a first-order approximation may be justified. The resultant equations are fairly complex and not easy to treat numerically, however, and the formulation is certainly not applicable to highly relativistic phenomena.

It should also be mentioned that several groups (Cardall et al. 2005, 2013; Peres et al. 2014) are developing different formulations for multi-D Boltzmann hydro simulations, which have yet to be implemented. Ott et al. (2008) performed detailed two-dimensional (2D) Boltzmann hydro supernova simulations in the post-bounce phase but they ignored SR effects. As shown later, consistent treatments of SR effects are indispensable to obtain correct behaviors in neutrino transfer. They are also the first step toward fully GR Boltzmann simulations, which will be needed to study more extreme phenomena such as black hole formations.

In this paper, we propose a novel formulation for the numerical computations of multi-D SR Boltzmann transfer based on the S_n method, which treats SR effects to all orders of v/c, where c and v denote the speed of light and fluid velocity, respectively. The accuracy of our new method is checked by the standard tests as well as by a realistic simulation of spherical collapse of a $15\,M_\odot$ progenitor. As explained in the next section, the appropriate treatment of SR effects is crucial for numerically capturing neutrino trapping and the subsequent evolution up to bounce. In this paper, we particularly focus on this issue, and more detailed quantitative analyses of realistic supernova simulations with our Boltzmann hydro code will be reported in subsequent papers.

This paper is organized as follows. To facilitate readers' understanding, we first give intuitive arguments on the importance of the SR effect from the perspective of phase space (in Section 2), which will make clear why non-relativistic (NR) Boltzmann hydro simulations fail to capture neutrino advections with matter and yield qualitatively wrong distributions of neutrinos. In Section 3, we also emphasize that the treatment of SR effects is not so easy practically, and we explain what the main obstacle is. Then the basic equations and formulations are presented in Section 4. After introducing two independent energy grids (which are essential for our SR treatment) in Section 5, the numerical algorithms are given in Section 6. We examine the accuracy of our new method using a series of SR Boltzmann and Boltzmann hydro simulations in Section 7. Finally we conclude the paper with a summary and discussion about further extensions of our code to a GR version in Section 8. Throughout this paper, Greek and Latin subscripts denote spacetime and space components, respectively. We use the metric signature of $-+++$. Unless otherwise stated, we work in units with $c = G = 1$, where G is the gravitational constant.

2. SR EFFECTS AND NEUTRINO TRAPPING

Before going into details of our SR Boltzmann formulation and its numerical algorithm, we first give intuitive arguments on the importance of SR effects. As will be observed below, the ignorance of SR effects yields qualitatively wrong behaviors in neutrino distributions. The key ingredient is the angular distribution in phase space: isotropic distributions in the fluid restframe become *anisotropic* in the laboratory frame after Lorentz transformations, a fact that ensures the advection of neutrinos with matter and eventually neutrino trapping.

In the following section, we will explain this process in a simplified and idealized setup. We consider neutrino transfer in moving matter that has uniform velocity and thermodynamic quantities. In addition, we assume that neutrinos and matter are strongly coupled with each other via scattering and, as a result, the neutrino distribution function in phase space, f, is isotropic in the fluid restframe, a situation similar to those we see locally in the neutrino trapping phase. Then the neutrino flux at each point vanishes in the fluid restframe and there is no net flux traversing the fluid elements (see the left panel in Figure 1). The neutrino number in each fluid element is conserved as the fluid element moves at finite velocity.

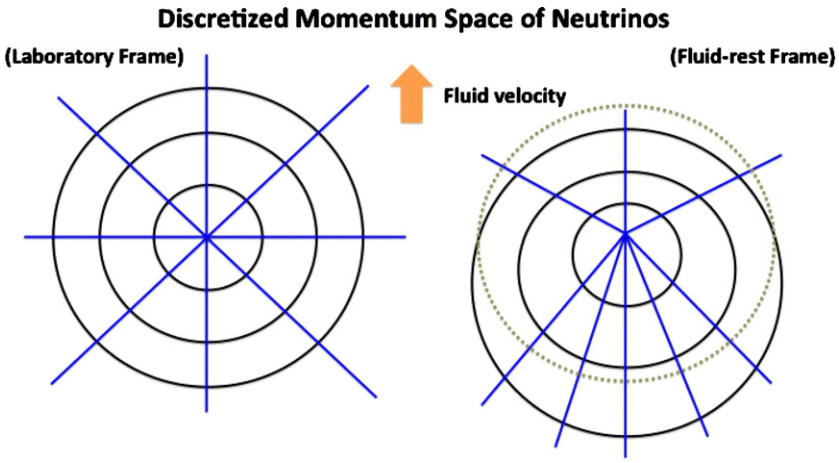

Figure 2. Left: discretized momentum space of neutrinos in the laboratory frame. Spherical coordinates are employed. The radial direction corresponds to neutrino energy and the azimuthal dimension is omitted. The grid in each dimension may not be uniform. Right: Lorentz-transformed mesh in the fluid restframe. The blue lines correspond to the radial lines whereas the black lines are transformed from the concentric circles in the left panel. The brown dots show an isoenergy circle in the fluid restframe for comparison. Matter is assumed to move upward in this figure.

(A color version of this figure is available in the online journal.)

This is the advection of neutrinos with matter and it should be evident why the Lagrangian approach is advantageous in dealing with it.

For comparison, the right panel in Figure 1 describes the same situation except in the laboratory frame. Here, we assume that the fluid is advected inward (or toward the left in the figure). Since the neutrinos should be advected in the same direction as the fluid in the laboratory frame, the incoming neutrino flux is larger than the outgoing one, which means that the angular distribution of neutrinos is *anisotropic* in this frame. From the SR point of view, such anisotropies arise from the Doppler shift and relativistic beaming by Lorentz transformations. The mathematical expression of SR Boltzmann equations will be given in Section 4.

If we neglected all SR effects, not distinguishing between the laboratory and fluid restframes, we would not obtain the neutrino advection with matter, which is crucial for neutrino trapping in the collapsing phase. In fact, neutrinos would be left behind as fluids are advected. The supernova core is not homogeneous in reality and both matter and neutrino densities are highest at the center. In the absence of advection, neutrinos would always flow outward when actually they should move inward, keeping pace with matter, and be effectively trapped in the core. As we will show later in Section 7.5, the number density of electron-type neutrinos becomes significantly smaller near the center for NR simulations. This, in turn, affects the evolution of the electron fraction and the size of inner core and eventually all the supernova dynamics thereafter.

3. DIFFICULTIES IN HANDLING SR EFFECTS

In this section, we give more detailed intuitive explanations about why SR treatments are not easy with the S_n method, which we employ in this paper. The main source of difficulty is scattering, particularly scattering between neutrinos and nucleons (and nuclei). There are no technical challenges, however, with other reactions such as neutrino absorptions and emissions.[5] We hence focus only on the isoenergetic scatterings in this section.

[5] Of course, non-isoenergetic scatterings of electrons and neutrinos and pair processes are another complication, which will be addressed in future work.

As mentioned in the previous sections, our Boltzmann hydro code is based on the Eulerian picture, and we discretize six-dimensional phase space in the laboratory frame, as shown in the left panel in Figure 2. In this picture, spherical coordinates in momentum space are adopted with the azimuthal dimension being collapsed. The radial direction corresponds to neutrino energy. Although the picture is drawn that way, gridding in each dimension is not necessarily uniform.

We first consider the isoenergetic scattering under the condition of fluid being at rest and, as a consequence, the laboratory frame coincides with the fluid restframe. When a neutrino undergoes isoenergetic scattering, it changes its flight direction specified by two angles, preserving energy. In the discretized momentum space, the neutrino moves from one bin to another with the same radial-grid number. The important thing is that only the angular grid number is changed. In this case, there is no difficulty and, indeed, this method has been implemented in Sumiyoshi & Yamada (2012) and Sumiyoshi et al. (2014).

In the presence of non-vanishing fluid velocities, the problem becomes qualitatively different. In this case, the laboratory frame is different from the fluid restframe and they are related to each other via a Lorentz transformation. The point is that the Lorentz transformation induces changes in both energy and angles. These energy shifts and aberrations are determined by the Doppler factor, which depends on the fluid velocity and neutrino angles (see Section 4). This is most clearly demonstrated in the right panel of Figure 2, in which the spherical coordinates given in the laboratory frame are Lorentz-transformed to the fluid restframe. It is evident that they are no longer spherically symmetric and distorted in the latter frame. This picture summarizes the difficulties in treating scatterings even if they are isoenergetic. As is well known, the neutrino distribution function, f, is a Lorentz invariant and its values at corresponding points in different frames are identical. The important point, however, is the fact that grid points are shifted by Lorentz transformations and concentric (equivalently isoenergetic) spheres in the laboratory frame are no longer spheres in the fluid restframe. As a consequence, some interpolations are inevitable when evaluating the collision terms for scatterings in the fluid restframe if one were to avoid the v/c expansion. There are, however, several challenges

with carrying out this interpolation, particularly with regard to neutrino energy. We briefly describe the reasons for these challenges.

The rather low energy resolution we can afford by using the Boltzmann code is one of the reasons. We can deploy at most ∼20 energy bins (see Kotake et al. 2012a). The distribution function, f, depends strongly on the neutrino energy in general. In particular, it decreases almost exponentially at high energies. On the numerical mesh, f may change several orders of magnitude between adjacent energy-grid points. Highly accurate interpolations of f are hence required on the coarse mesh. Note that since the isoenergetic scatterings between neutrinos and nucleons and/or nuclei dominate other reactions in CCSNe, the time step (Δt) of simulations is mostly determined by these processes. If the interpolations of f are not accurate at high energies, we might find that Δt becomes unreasonably small because of a large number of artificial scatterings. The fact that high-energy neutrinos have larger cross sections makes matter worse. Not to mention, in the interpolation we further have to take into consideration the conservation of neutrino numbers in scatterings.

In the next section, we give the SR Boltzmann equations then we present our plan for overcoming the challenged faced by implementing them. We then demonstrate our successful handling of isoenergetic scatterings in the realistic supernova simulations (see Section 7).

4. SR BOLTZMANN EQUATIONS FOR NEUTRINOS

We start with the covariant form of the Boltzmann equation:

$$p^\mu \frac{\partial f}{\partial x^\mu} + \frac{dp^i}{d\tau}\frac{\partial f}{\partial p^i} = \left(\frac{\delta f}{\delta \tau}\right)_{\rm col}, \tag{1}$$

which is valid even in curved spacetime. In the above expression, $f(= f(x^\mu, p^i))$ denotes the neutrino distribution function in phase space; x^μ and p^μ are spacetime coordinates and the four-momentum of a neutrino, respectively. Since the latter satisfies the on-shell condition $p^\mu p_\mu = -m_\nu^2$, in which m_ν is a neutrino mass, only three of the four components are independent and this is why only spatial components appear in the second term on the left-hand side; τ stands for the affine parameter of the neutrino trajectory. The left-hand side of Equation (1) expresses a geodesic motion in the phase space, while the right-hand side symbolically denotes the so-called collision terms, i.e., the terms that give the rate of changes in f due to neutrino–matter interactions.

On the spherical coordinates in flat spacetime, which are the coordinates we employ for the laboratory frame in our Eulerian approach, Equation (1) is cast into the following conservation form:

$$\begin{aligned}&\frac{\partial f}{\partial t} + \frac{\mu_\nu}{r^2}\frac{\partial}{\partial r}(r^2 f) + \frac{\sqrt{1-\mu_\nu^2}\cos\phi_\nu}{r\sin\theta}\frac{\partial}{\partial\theta}(\sin\theta f)\\ &\quad + \frac{\sqrt{1-\mu_\nu^2}\sin\phi_\nu}{r\sin\theta}\frac{\partial f}{\partial\phi} + \frac{1}{r}\frac{\partial}{\partial\mu_\nu}[(1-\mu_\nu^2)f]\\ &\quad - \frac{\sqrt{1-\mu_\nu^2}}{r}\frac{\cos\theta}{\sin\theta}\frac{\partial}{\partial\phi_\nu}(\sin\phi_\nu f) = \left(\frac{\delta f}{\delta t}\right)_{\rm col}^{\rm lb},\end{aligned} \tag{2}$$

where r, θ, and ϕ denote the spatial variables. For the three independent components of neutrino four-momentum, we do not use the spacial components but adopt the energy and two angles, θ_ν and ϕ_ν (see Figure 3). μ_ν is defined as $\mu_\nu \equiv \cos\theta_\nu$.

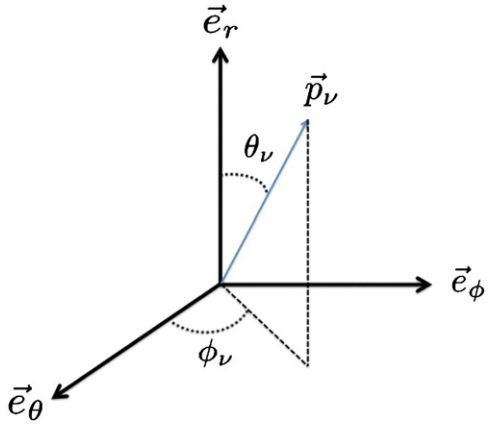

Figure 3. Local orthonormal bases that measure neutrino momentum. As the subscripts show, $\boldsymbol{e}_r$, $\boldsymbol{e}_\theta$, and $\boldsymbol{e}_\phi$ are aligned with the spatial spherical coordinates. (A color version of this figure is available in the online journal.)

In Equation (2) and the rest of this paper, we assume that neutrinos are massless, which is well justified as long as neutrino oscillations are ignored.

The collision term in Equation (2), which is expressed with the laboratory time t, is related to the original collision term in Equation (1) as

$$\left(\frac{\delta f}{\delta \tau}\right)_{\rm col} = \varepsilon^{\rm lb}\left(\frac{\delta f}{\delta t}\right)_{\rm col}^{\rm lb}, \tag{3}$$

where $\varepsilon^{\rm lb}(\equiv p^t)$ denotes the neutrino energy measured in the laboratory frame. Similarly, the collision term in the fluid restframe can be expressed with the proper time of each fluid element ($\tilde{t}$) as

$$\left(\frac{\delta f}{\delta \tau}\right)_{\rm col} = \varepsilon^{\rm fr}\left(\frac{\delta f}{\delta \tilde{t}}\right)_{\rm col}^{\rm fr}, \tag{4}$$

where $\varepsilon^{\rm fr}(\equiv p^{\tilde{t}} \equiv -u_\mu p^\mu)$ denotes the neutrino energy in the fluid restframe. Here u^μ is the four-velocity of matter.

The Lorentz transformation of four-momentum gives the relation of neutrino energies in the fluid restframe and laboratory frame as

$$\varepsilon^{\rm fr} = \varepsilon^{\rm lb}\gamma(1 - \boldsymbol{n}^{\rm lb}\cdot\boldsymbol{v}), \tag{5}$$

where $\boldsymbol{v}$, $\gamma(\equiv (1-v^2)^{-1/2})$ denote the three-velocity and corresponding Lorentz factor of matter and $\boldsymbol{n}^{\rm lb}$ is the unit vector that indicates the flight direction of a neutrino in the laboratory frame. The factor $D^{\rm lb} \equiv \gamma(1-\boldsymbol{n}^{\rm lb}\cdot\boldsymbol{v})$ in Equation (5) expresses the Doppler shift of neutrino energy. From Equations (3)–(5), we can obtain the relation between the collision terms in the two frames as

$$\left(\frac{\delta f}{\delta t}\right)_{\rm col}^{\rm lb} = D^{\rm lb}\left(\frac{\delta f}{\delta \tilde{t}}\right)_{\rm col}^{\rm fr}. \tag{6}$$

The Lorentz transformation also gives the relation between the flight directions in the fluid restframe and laboratory frames as

$$\varepsilon^{\rm fr}\boldsymbol{n}^{\rm fr} = \varepsilon^{\rm lb}\left[\boldsymbol{n}^{\rm lb} + \left\{-\gamma + (\gamma-1)\frac{\boldsymbol{n}^{\rm lb}\cdot\boldsymbol{v}}{v^2}\right\}\boldsymbol{v}\right]. \tag{7}$$

Here $\boldsymbol{n}^{\rm fr}$ denotes the unit vector that specifies the flight direction of a neutrino in the fluid restframe. Using the Doppler factor

$D^{\rm lb}$, we obtain

$$\boldsymbol{n}^{\rm fr} = \frac{1}{D^{\rm lb}}\left[\boldsymbol{n}^{\rm lb} + \left\{-\gamma + (\gamma-1)\frac{\boldsymbol{n}^{\rm lb}\cdot\boldsymbol{v}}{v^2}\right\}\boldsymbol{v}\right]. \quad (8)$$

Note that this relation no longer contains neutrino energy and the angle transformations are decoupled from the energy transformations. This is a great simplification, which we make full use of in the following section, and is a consequence of the assumption that neutrinos are massless. The solid angle element is then transformed as

$$d\Omega^{\rm fr} = \frac{1}{(D^{\rm lb})^2} d\Omega^{\rm lb}. \quad (9)$$

In the Boltzmann equation, neutrino–matter interactions are described in the collision terms. As is well known, they are obtained most easily in the fluid restframe. We hence evaluate the collision term in this frame and use Equation (6) to obtain the expression in the laboratory frame. The interactions that we take into account in this paper are the same as those in Sumiyoshi & Yamada (2012), the minimum set for supernova simulations. Since Sumiyoshi & Yamada (2012) worked in the Newtonian approximation, we need the following replacements to employ their collision terms:

$$\begin{aligned}\left[\frac{1}{c}\frac{\delta f}{\delta t}\right] &\rightarrow \left(\frac{\delta f}{\delta \tilde{t}}\right)^{\rm fr}_{\rm col},\\ \varepsilon &\rightarrow \varepsilon^{\rm fr},\\ \Omega &\rightarrow \Omega^{\rm fr},\\ R_* &\rightarrow R_*^{\rm fr},\end{aligned} \quad (10)$$

where R_* denotes reaction kernels.

Here we take the collision terms for the isoenergetic scatterings in the laboratory frame and see how the number of neutrinos conserved is preserved, which will be useful in the next section. Following Sumiyoshi & Yamada (2012) and implementing the above replacements, we can write the terms as

$$\left(\frac{\delta f}{\delta \tilde{t}}\right)^{\rm fr}_{\rm scat}(\varepsilon^{\rm fr},\Omega^{\rm fr}) = -\frac{(\varepsilon^{\rm fr})^2}{(2\pi)^3}\int d\Omega'^{\rm fr} R^{\rm fr}_{\rm scat}(\Omega^{\rm fr},\Omega'^{\rm fr}) \times (f^{\rm fr}(\varepsilon^{\rm fr},\Omega^{\rm fr}) - f^{\rm fr}(\varepsilon^{\rm fr},\Omega'^{\rm fr})), \quad (11)$$

where $R^{\rm fr}_{\rm scat}$ and $f^{\rm fr}$ denote the isoenergetic scattering kernel and neutrino distribution function f in the fluid restframe, respectively. The integration of Equation (11) over the solid angle $\Omega^{\rm fr}$ vanishes due to symmetric properties of the scattering kernel: $R(\Omega,\Omega') = R(\Omega',\Omega)$. This represents the conservation of the number of neutrino for the isoenergetic scatterings at each energy in the fluid restframe.

5. TWO ENERGY GRIDS

The origin of the difficulties in the treatment of SR is the fact that the neutrino momentum space is distorted by Lorentz transformations, i.e., the isoenergy surfaces in the laboratory frame do not coincide with the counterparts in the fluid restframe. We then need highly accurate interpolations in the energy of f, taking care to conserve the number of neutrinos, whose difficulties in the S_n method were elucidated in Section 3.

We overcome these difficulties by not employing the grid shown in the left panel of Figure 2 but the so-called Lagrangian remapped grid (hereafter LRG) in the laboratory frame, which is Lorentz-transformed from the fluid restframe. It is emphasized that LRG is the one we mainly use in our Eulerian approach. In Figure 4, we display the schematic picture of our LRG (see also Figure 2 for comparison). In this method, the energy grid is constructed so that it should be isotropic in the fluid restframe.

As a consequence, it becomes anisotropic in the laboratory frame as observed in the left panel. The energy grids obtained that way in the laboratory frame are different from point to point at each time and also change in time because of inhomogeneous fluid motions. Thanks to the isotropic energy grids in the fluid restframe, no special care is needed in the treatment of the isoenergetic scatterings on this grid. Note that the angular mapping is independent of energy. The angular grid is constructed, on the other hand, so that it should be uniform in the laboratory frame. It implies that the angular mesh is non-uniform in the fluid restframe as shown in the right panel. In contrast to the energy grid, the non-uniform angular grid in the fluid restframe causes no practical problems (see Equation (32) for the correction by angular aberration).

One might say that the Lagrangian remapping method is simply the canonical Lagrangian approach, but there are several differences between the two. One of the important differences lies in the treatment of advection terms on the left-hand side of the Boltzmann equation. As we have already mentioned in Section 1, the advection terms are fairly complicated in the Lagrangian approach due to the spatial inhomogeneities and temporal changes of matter velocity. We demonstrate this in a simplified situation in Figure 5. Here, we consider neutrinos propagating outward (or rightward in the figure) in optically thin matter. We further assume that the matter is moving inward (or leftward in the figure) at velocities that are piecewise constant with $|v_{\rm Left}| < |v_{\rm Right}|$ (see the bottom panel in this figure). The discontinuity may be regarded as a standing shock wave.

In this situation, the neutrino energy spectrum in the laboratory frame is uniform in space since neutrinos are not interacting with matter at all (see the upper picture).[6] This is not the case in the fluid restframe, however. It is, in fact, blueshifted at the discontinuity of matter velocity (see the middle picture in Figure 5). In the Lagrangian picture, such energy shifts are expressed as the advection in energy space and given by the partial derivative with respect to energy on the left-hand side of the Boltzmann equation. In the present case, there should be an infinite energy flux at the discontinuity.[7] In our Lagrangian remapping method, on the other hand, we work in the laboratory frame, in which the energy grid is anisotropic as shown in the left panel of Figure 4 and the blueshift in the spectrum is just compensated for by the contraction of the energy grid in the outward direction and, as a consequence, the energy spectrum is unchanged across the discontinuity (see the upper picture in Figure 5).

It is easily understood that the use of LRG, which is anisotropic and spatially non-uniform, complicates the calculation of spatial and neutrino-angular advection, a problem similar to that in the ordinary Lagrangian method. This is mitigated in our method, however, by the introduction of yet another energy grid, which is isotropic and identical at all spatial grid points in the laboratory frame (referred to hereafter as the laboratory fixed grid, or LFG; see also Section 6.4 for more details). LFG is employed only to calculate the neutrino advection. Note that

[6] It is assumed here that the boundary condition is fixed and a steady state has been established.

[7] In numerical simulations, such a discontinuity is somewhat smeared and the flux always becomes finite.

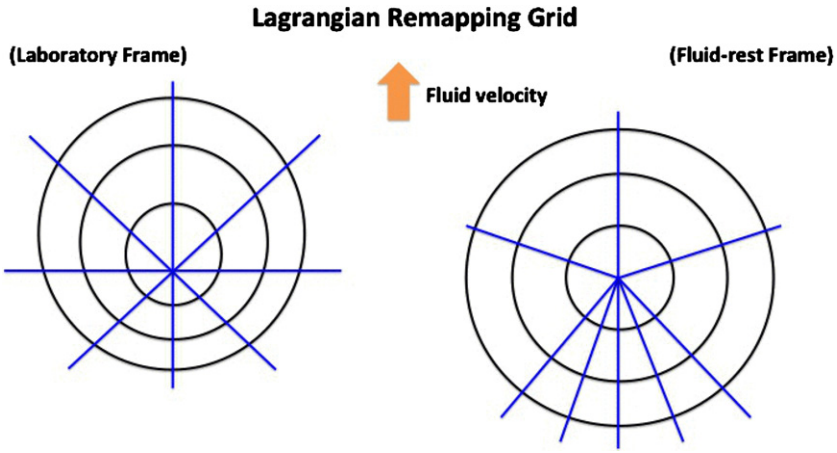

Figure 4. Lagrangian remapped grid in the laboratory frame (left panel) and the Lorentz-transformed grid in the fluid restframe (right panel). The energy grid is isotropic in the fluid restframe whereas it becomes anisotropic in the laboratory frame. The angular grid, on the other hand, is uniform in the laboratory frame.
(A color version of this figure is available in the online journal.)

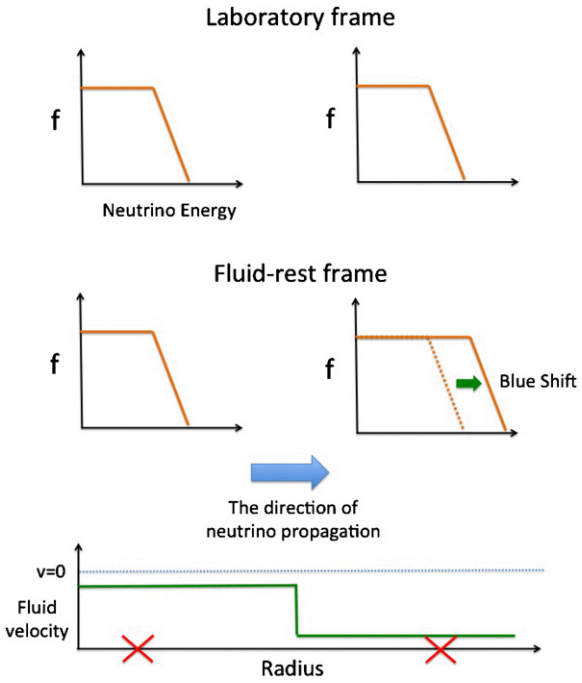

Figure 5. Schematic pictures of the energy spectra of outgoing neutrinos in the laboratory (upper) and fluid restframes (middle). Matter is assumed to be optically thin and flows inward at piecewise constant velocities with a discontinuity in the middle (lower picture). The two red crosses in the bottom picture are the locations where we measure the neutrino spectra. The spectrum should be unchanged across the discontinuity in the laboratory frame whereas it will be blueshifted in the fluid restframe.
(A color version of this figure is available in the online journal.)

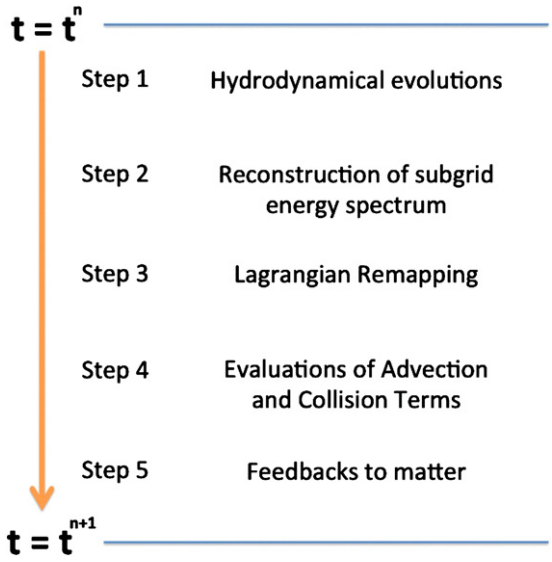

Figure 6. Flow chart for our Boltzmann hydro solver.
(A color version of this figure is available in the online journal.)

as long as we work in the laboratory frame, energy-derivative terms do not appear explicitly on the left-hand side of the Boltzmann equation and the advection on the LFG is particularly simple. It should be repeated that the LFG is a grid only for temporary use to treat the neutrino advection. Accordingly, f on the LFG, which is obtained by interpolation in our method, is also a temporal variable. Instead, f on the LRG is the quantity to be solved and stored in our code.

6. NUMERICAL IMPLEMENTATIONS

In this section, we explain the detailed numerical algorithm used to implement the various elements described above in our Boltzmann hydro solver, paying particular attention to the usage of different energy grids. Figure 6 summarizes the multiple steps needed to update a numerical solution from $t = t^n$ to t^{n+1}, where the superscripts represent the time steps. In the following sections, we provide detailed descriptions of each step in sequential order.

6.1. Step 1: Hydrodynamical Evolutions

In our Boltzmann hydro solver, operator splitting is employed. We first compute hydrodynamics, neglecting neutrino interactions, i.e., in an adiabatic manner, then from Steps 2 through 4, we perform neutrino transfer for the matter distribution given in the first step. Feedback from neutrino interactions to the internal energy, velocity, and electron fraction of matter are taken into account in Step 5.

The numerical code for hydrodynamical evolution is essentially the same as that in Nagakura et al. (2013). It is based on the so-called central scheme with an explicit time evolution (Kurganov & Tadmor 2000; Nagakura & Yamada 2008; Nagakura et al. 2011). The code was successfully applied to the simulations of standing accretion shock instability in the

post-bounce phase in our previous study (Nagakura et al. 2013). It is also noted that a series of standard tests for hydrodynamical schemes (e.g., shock tube problems) were carried out in Nagakura et al. (2011).

Although our Boltzmann solver is fully SR, the hydrodynamics solver is Newtonian. As a matter of fact, it can be GR-Hydro code (Nagakura & Yamada 2008) except for its gravity solver, which is Newtonian and based on the MICCG technique (Nagakura et al. 2011). The implementation of an Einstein equation solver is currently underway, the perspective of which will be mentioned in Section 8.

The basic equations of Newtonian hydrodynamics in spherical coordinates are written in the following form:

$$\partial_t \boldsymbol{Q} + \partial_j \boldsymbol{U}^j = \boldsymbol{W_h} + \boldsymbol{W_i}, \tag{12}$$

where each term is given as

$$\boldsymbol{Q} = \begin{pmatrix} \sqrt{g}\rho \\ \sqrt{g}\rho v_r \\ \sqrt{g}\rho v_\theta \\ \sqrt{g}\rho v_\phi \\ \sqrt{g}(e + \frac{1}{2}\rho v^2) \\ \sqrt{g}\rho Y_e \end{pmatrix}, \tag{13}$$

$$\boldsymbol{U}^j = \begin{pmatrix} \sqrt{g}\rho v^j \\ \sqrt{g}(\rho v_r v^j + p\delta_r^j) \\ \sqrt{g}(\rho v_\theta v^j + p\delta_\theta^j) \\ \sqrt{g}(\rho v_\phi v^j + p\delta_\phi^j) \\ \sqrt{g}(e + p + \frac{1}{2}\rho v^2)v^j \\ \sqrt{g}\rho Y_e v^j \end{pmatrix}, \tag{14}$$

$$\boldsymbol{W_h} = \begin{pmatrix} 0 \\ \sqrt{g}\rho\left(-\psi_{,r} + r(v^\theta)^2 + r\sin^2\theta(v^\phi)^2 + \frac{2p}{r\rho}\right) \\ \sqrt{g}\rho\left(-\psi_{,\theta}r^2 + \sin\theta\cos\theta(v^\phi)^2 + \frac{p\cos\theta}{\rho\sin\theta}\right) \\ -\sqrt{g}\rho\psi_{,\phi} \\ -\sqrt{g}\rho v^l\psi_{,l} \\ 0 \end{pmatrix}, \tag{15}$$

$$\boldsymbol{W_i} = \begin{pmatrix} 0 \\ -\sqrt{g}G^r \\ -\sqrt{g}G^\theta \\ -\sqrt{g}G^\phi \\ -\sqrt{g}G^t \\ -\sqrt{g}\Gamma \end{pmatrix}. \tag{16}$$

Note that $\boldsymbol{W_i}$ corresponds to the interactions between neutrinos and matter (the explicit expressions will be presented in Step 5) and $\sqrt{g}(= r^2\sin\theta)$ denotes the volume factor in the spherical coordinates. Other variables, ρ, p, e, Y_e, v^j, and ψ, are the mass density, pressure, internal energy density, electron fraction, fluid velocity, and Newtonian gravitational potential, respectively. The Newtonian self-gravity is solved with the Poisson equation,

$$\Delta\psi = 4\pi\rho. \tag{17}$$

In our central scheme, the above system of equations use the finite difference method in space with a piecewise parabolic method interpolation and the total variation diminishing Runge–Kutta method is employed for time integration, which achieves second-order accuracy in both space and time. We adopt the procedure proposed by Müller et al. (2010) for solving the energy equation (the fifth component in Equation (12)), which reduces secular errors in the energy conservation.

Throughout this paper, we use Shen's equation of state (EOS; Shen et al. 2011) with lepton and photon contributions added. (see, e.g., Nagakura et al. 2013). The original EOS table is rather coarse for the simulation of CCSNe. Indeed, we have found that trilinear interpolations in the original table reduce the accuracy of simulations, particularly at the transition from inhomogeneous to homogeneous nuclear matter. We have hence reconstructed a new EOS table by interpolating all quantities with the tricubic Hermite functions. It is several times finer in ρ, Y_e and T than the original table.

6.2. Step 2: Reconstruction of Subgrid Energy Spectrum

In our Boltzmann solver, transformations between different energy grids are frequently performed. As mentioned in Section 3, we will be able to deploy at most ∼20 energy bins, a rather coarse resolution. We hence need a subgrid modeling of the neutrino energy spectrum. It is also important for computing flux at grid boundaries. As a matter of fact, if we did not take into account such subgrid distributions and assumed instead that neutrinos are populated uniformly in each grid, then a large number of neutrinos could artificially leak to neighboring grids either due to inaccurate numerical flux or by imprecise interpolations (see also Step 4 on this issue).

In the reconstruction, one should pay adequate attention to the following two conditions:

1. monotonicity and
2. conservation of the number of neutrinos.

The first condition is familiar in the numerical treatment of hyperbolic systems and necessary to avoid artificial generation of extrema in spectra, which may cause numerical instabilities. The importance of the second condition is rather obvious. In fact, if it were violated, neutrinos would appear or disappear just by changing energy grids. As shown later, this condition is particularly important in the evaluation of f on LFG. Note that the value of f on each grid point actually represents the average in the energy bin in our formulation.

The reconstruction procedures are schematically shown in Figure 7, in which we construct the subgrid energy spectrum for energy bin A in the LRG. In so doing, not only grid point A but also the neighboring grid points B and C are utilized. We distinguish two cases: (1) f locally takes an extreme value on grid point A, i.e., both of the f's on grid points B and C are either larger or smaller than the f on grid point A and (2) when this is not the case.

The left panels in Figure 7 correspond to the first case. As shown in the figure, in this case, we assume a flat spectrum in the energy bin. This is not a bad approximation since the actual spectrum is indeed nearly flat in the vicinity of a local extremum. In the second case, in which f changes monotonically over the neighboring three grid points, we reconstruct a subgrid spectrum as follows, which is shown in the right panels in Figure 7.

We first determine the value of f on the left and right interfaces of energy bin A as the averages of adjacent grid point values in the logarithmic scale. They are referred to as $f_{\rm L}$ ($f_{\rm R}$), respectively. We also define $f_{\rm max}$ and $f_{\rm min}$ as the largest

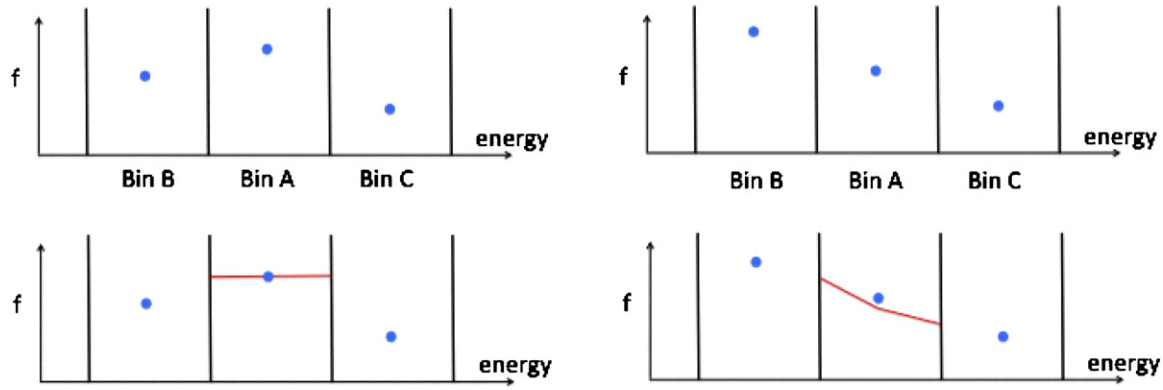

Figure 7. Reconstruction of the subgrid energy spectrum on LRG. The upper panels show two representative distributions of grid point values of f (blue filled circles) for three consecutive energy bins. The lower panels present the reconstructed subgrid spectra (red lines) in bin A for the two cases. If the grid point value in energy bin A takes a local minimum or maximum among the three grid points (left panels), then we assume a uniform subgrid spectrum. Otherwise, we construct the subgrid spectrum iteratively (right panels). See the text for details.

(A color version of this figure is available in the online journal.)

(smallest) of $f_{\rm L}$ and $f_{\rm R}$. Denoting the grid point value of f by $f_{\rm m}$, we first construct a trial spectrum $f_{\rm tmp}$ as follows:

$$f_{\rm tmp}(\varepsilon) = \frac{1}{e^{G(\varepsilon)}+1} \tag{18}$$

$$G(\varepsilon) = \begin{cases} \frac{G_{\rm L}-G_{\rm m}}{\varepsilon_{\rm L}-\varepsilon_{\rm m}}(\varepsilon-\varepsilon_{\rm m})+G_{\rm m} & (\varepsilon < \varepsilon_{\rm m}), \\ \frac{G_{\rm R}-G_{\rm m}}{\varepsilon_{\rm R}-\varepsilon_{\rm m}}(\varepsilon-\varepsilon_{\rm m})+G_{\rm m} & (\varepsilon > \varepsilon_{\rm m}), \end{cases} \tag{19}$$

where $\varepsilon_{\rm L}$, $\varepsilon_{\rm R}$, and $\varepsilon_{\rm m}$ are the energies at the left and right interfaces and grid point, respectively; $G_{\rm L}$, $G_{\rm R}$, and $G_{\rm m}$ are the corresponding values of G given as

$$G_{\rm i} \equiv \log\left(\frac{1}{f_{\rm i}}-1\right) \quad (i = {\rm L}, {\rm R}, {\rm m}). \tag{20}$$

It is clear that this expression becomes exactly correct if neutrinos are in thermal equilibrium and take a Fermi–Dirac distribution.

It is obvious, however, that $f_{\rm tmp}(\varepsilon)$ does not ensure that the number of neutrinos is conserved. Hence we need to modify $f_{\rm tmp}(\varepsilon)$. We first integrate $f_{\rm tmp}$ in the energy bin to obtain the number of neutrinos, $N_{\rm A}^{'}$, in it. This should be equal to $N_{\rm A}$, the true value. Using the ratio,

$$R_{\rm rate} \equiv \frac{N_{\rm A}}{N_{\rm A}^{'}}, \tag{21}$$

we scale the temporary spectrum as $f_{\rm tmp} \times R_{\rm rate}$ to obtain a new subgrid spectrum, which by definition satisfies the conservation of neutrinos exactly.

The new spectrum so obtained does not satisfy the general monotonicity condition, which requires that f should always be between $f_{\rm max}$ and $f_{\rm min}$. Hence we apply a limiter if $f_{\rm tmp}$ exceeds $f_{\rm max}$ and/or $f_{\rm min}$: $f_{\rm tmp}$ is modified so that both components are within the acceptable range. Owing to this limiter, the value of $N_{\rm A}^{'}$ obtained by integrating the new subgrid spectrum again deviates from $N_{\rm A}$. We repeat the above procedure until the following condition is satisfied:

$$|1 - R_{\rm rate}| < \epsilon_{\rm conv}, \tag{22}$$

where $\epsilon_{\rm conv}$ is a measure of convergence and is set to $\epsilon_{\rm conv} = 10^{-3}$. It is important that the convergence of this iteration is guaranteed mathematically and that no artificial extremum emerges in the reconstructed spectrum.

6.3. Step 3: Lagrangian Remapping

Here we carry out the Lagrangian remapping of neutrino energy grids and compute the change in f on the LRG. The subgrid energy spectrum, which is obtained in the previous step, plays an important role in this process.

The procedure is summarized in Figure 8. Suppose that n time integrations have been finished and all quantities associated with matter and neutrinos have been obtained at $t = t^n$. The upper panel shows the grid point values of f as well as subgrid spectra in three consecutive energy bins on the LRG at $t = t^n$. Note that the angular dimensions are suppressed in the figure. In Step 1, matter velocities are changed. As explained in Section 5, the LRG is determined so that the neutrino energy grid is identical in each instantaneous fluid restframe. We hence need to update the LRG accordingly as shown with green lines in the middle panel of Figure 8. It is then evident that f should be also changed on account of the shifts of the grid boundaries. As shown in the figure, neutrinos in the shaded areas determine the change of f due to this remapping.

To evaluate the numbers of neutrinos in these regions, we use $f_{\rm int}$, the interface value of f on the old LRG at $t = t^n$. It is obtained as the smaller of the two interface values derived from the subgrid spectra in the adjacent grids in order to prevent the moving of too many neutrinos. With this $f_{\rm int}$ and the energies at the grid interfaces on the old ($\varepsilon_{\rm old}$) and new ($\varepsilon_{\rm new}$) LRGs, the number of neutrinos to be moved to the adjacent grid ΔN_ν is given by

$$\Delta N_\nu = f_{\rm int}\frac{1}{3}|(\varepsilon_{\rm new})^3 - (\varepsilon_{\rm old})^3|\Delta\Omega, \tag{23}$$

where $\Delta\Omega$ is the extent of solid angle of the bin.[8] Note that the conservation of the number of neutrinos is automatically guaranteed in this process. We end this step with a construction of the subgrid spectrum for the modified number of neutrinos (and accordingly f) in each energy bin in the same way as in Step 2.

[8] Note again that we suppress the angular dimension in Figure 8.

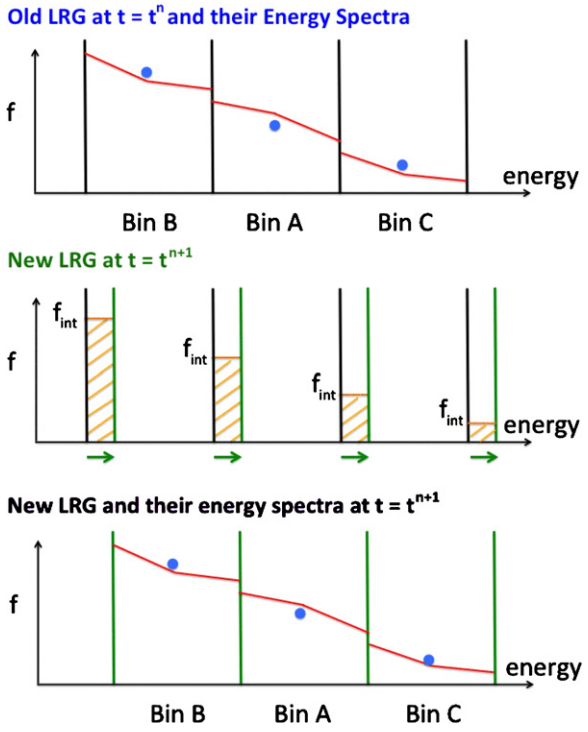

Figure 8. Lagrangian remapping. The upper panel shows the grid-center values of f and the reconstructed subgrid energy spectra on the LRG at $t = t^n$. The middle panel compares the LRG's at $t = t^n$ (black lines) and $t = t^{n+1}$ (green lines). Arrows indicate the shifts of grid interfaces. Neutrinos in the shaded regions should change their affiliations to the neighboring grids (see the text for more details). The lower panel displays the grid center values of f and the reconstructed subgrid spectra on the new LRG at $t = t^{n+1}$.

(A color version of this figure is available in the online journal.)

We emphasize that up to this point, no interactions of neutrinos with matter have been taken into account. The change in f considered above is induced by the acceleration or deceleration of matter (and hence of the local fluid restframe). As explained in detail in Section 5, if such a change in matter velocity occurred in optically thin matter, the neutrino energy spectrum should not change in the laboratory frame. In our method, the red- or blueshifts of the energy spectrum in the fluid restframe are compensated for by the Lagrangian remapping. It should also be noted that the energy shift is proportional to the time step Δt and, as a consequence, it is small, a fact that is true even in the shock wave. This not only justifies the above estimation of ΔN_ν but also is a huge advantage in the use of the LRG compared with other Lagrangian formulations in which large energy shifts may occur.

6.4. Step 4: Evaluations of the Advection and Collision Terms

Now that the energy shift induced by matter motions has been treated, the remaining task is to consider the spatial advections and collisions of neutrinos. The latter is easy on the LRG, which is essentially the comoving grid, and will be briefly explained at the end of this section. The former, on the other hand, is fairly complicated, since the LRG is not uniform in space. In contrast to the ordinary Lagrangian formulation, in which the spatial advection is expressed as complicated partial derivatives, our method utilizes the fact that the advection is very simple in the laboratory frame. The LFG, which is defined in Section 5, is the main tool here.

As explained in Section 5, the LFG is defined so that the energy grids are identical everywhere in space and it does not depend on the flight direction of a neutrino. In addition, the LFG should have the following properties:

1. the LFG covers the union of all energy ranges in the LRG.[9]
2. Each energy bin in the LRG is covered by more than one energy bin in the LFG.

These conditions are important to ensure accuracy in the evaluation of the advection terms. Figure 9 displays an example of the relation between the two grids in the laboratory frame.

Given LFG, we evaluate the advection term as follows. We suppose that the nth time step has been completed and f^n is given on each LRG and the subgrid spectrum has also been constructed according to Step 2 (see panel a in Figure 10). Using this subgrid spectrum, which is denoted by $f_{\rm sub}$ in this section, we assign an f to each grid point in the LFG, which is denoted as $f_{\rm LF}$:

$$f_{\rm LF} \equiv f_{\rm spe}(\varepsilon_{\rm LFm}), \tag{24}$$

where $\varepsilon_{\rm LFm}$ corresponds to the neutrino energy at the grid point in the LFG (see panel (b) in the same figure, in which LFG is presented in green while LRG is shown with black dots.). Here we would like to emphasize again that the spatial and angular advection[10] terms on the LFG (the left-hand side of Equation (2)) are very simple. In fact, we can employ the same method as used in Sumiyoshi & Yamada (2012).[11]

Once the numerical fluxes for the spatial and angular advections are obtained on the LFG, we then calculate the corresponding numerical fluxes for the LRG as follows. We take as an example panel (b) in Figure 10. As mentioned earlier, the LFG is finer than the LRG. Energy bin A in LRG, for instance, is covered by three bins—C′, D′, and E′—in the LFG. Let us look at bin E′ in the LFG, which overlaps with bins A and C in the LRG. The numerical flux in the LFG should hence be shared with the latter two bins in the LRG. For that purpose, we introduce a factor, γ and divide the numerical flux $F_{E'}$ into $\gamma F_{E'}$ and $(1-\gamma)F_{E'}$. γ is defined as

$$\gamma \equiv \frac{N_{\rm L}}{N_{\rm L}+N_{\rm R}}, \tag{25}$$

with

$$N_{\rm L(R)} = \left|\left(\varepsilon^3_{\rm AC} - \varepsilon^3_{\rm L(R)}\right)\right| f_{\rm A(B)}, \tag{26}$$

where $\varepsilon_{\rm AC}$ is the neutrino energy at the interface of bins A and C in the LRG and $\varepsilon_{\rm L(R)}$ is the energy at the left (right) boundary of bin E′ in LFG; $f_{\rm A(B)}$ is the grid point value of f for bin A(B) in the LRG. The numerical flux for bin A of the LRG is a sum of the contributions from bins C′, D′, and E′ in the LFG, each obtained in this manner.

So far, we have explained our treatment of the spatial and angular advection terms as if the finite difference method were applied explicitly in time. As a matter of fact, we treat them implicitly in our method. This is important from a point of view

[9] Note that the energy range covered by the LRG depends on the spatial position and flight direction.

[10] Hereafter the angular advections mean the advection of neutrinos in the 2D momentum subspace spanning all flight directions.

[11] In this method the upwind and central finite differences are interpolated according to the optical depth. In so doing, we introduce the weighting factor, β, which is linearly interpolated from the LRG to the LFG in the present formulation. Since β takes a value in the range of 0.5–1 and does not strongly depend on the neutrino energy, unlike f, the simple linear interpolation is justified.

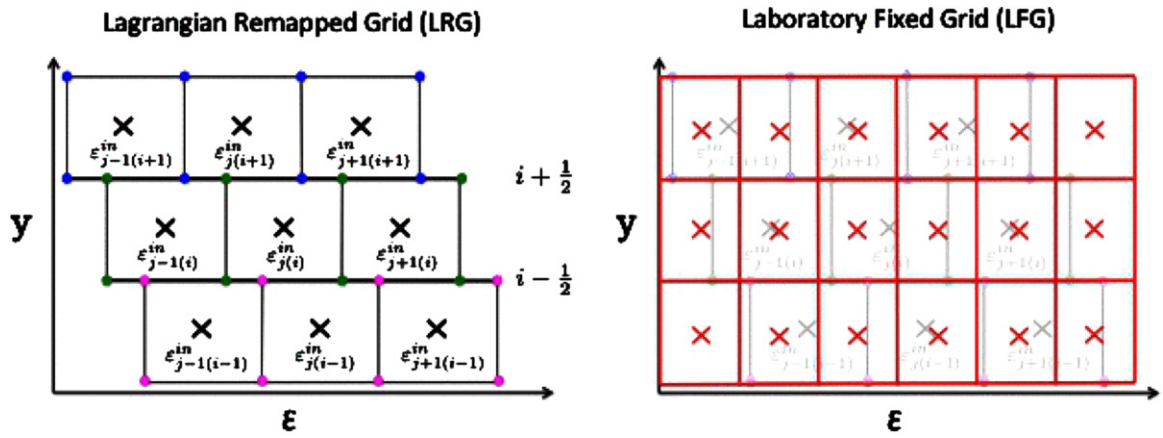

Figure 9. Left: energy bins in the LRG at neighboring spatial or angular points. y denotes a spatial or angular dimension whose grid points are specified by the subscript i. The subscript j indicates the energy grid points. Right: the same as the left panel but in the LFG (red rectangles). For comparison, the energy bins and grid points in the LRG are also displayed in gray in this panel.

(A color version of this figure is available in the online journal.)

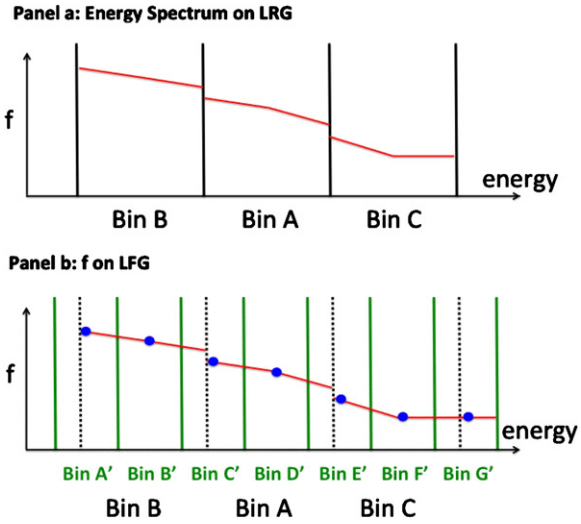

Figure 10. Upper panel: the subgrid energy spectrum on the LRG at $t = t^n$. Lower panel: the same as the upper panel but on the LFG (shown in green). For comparison, the LRG is displayed with dotted lines. The blue filled circles represent the grid point values of f on the LFG.

(A color version of this figure is available in the online journal.)

of numerical stability and computational times. The detailed procedure is as follows.

We first rewrite the Boltzmann equation (Equation (2)) as

$$\frac{\partial f}{\partial t} + \sum_k F^k_{\rm adv}(f) = \left(\frac{\delta f}{\delta t}\right)^{\rm lb}_{\rm col}(f), \tag{27}$$

in which the second term on the left-hand side is the sum of the spatial and angular advection terms. Since the following treatment is common to each term in the sum, we drop the subscript k hereafter.

In the implicit approach, both the advection and collision terms are evaluated at $t = t^{n+1}$ and the finite difference equation is written as

$$\frac{f^{n+1} - f^n}{\Delta t} = -F_{\rm adv}(f^{n+1}) + \left(\frac{\delta f}{\delta t}\right)^{\rm lb}_{\rm col}(f^{n+1}). \tag{28}$$

We note, however, that $F_{\rm adv}$ in SR is evaluated via the complex interpolation of f between the LFG and the LRG and is nonlinear and highly complicated. This prevents us from even linearizing the equation[12] and the implicit treatment of advection terms seems impossible.

It is noteworthy, however, that in the Newtonian approximation, in which no distinction is made between the fluid rest-frame and the laboratory frame, the advection term is linear and can be treated completely implicitly. In fact, the resultant NR equation can be cast into the following form (see also Sumiyoshi & Yamada 2012):

$$F^{\rm NR}_{\rm adv}(f^{n+1}) = A f^{n+1}_{(i)} + B f^{n+1}_{(i+1)} + C f^{n+1}_{(i-1)}, \tag{29}$$

where $F^{\rm NR}_{\rm adv}$ is the NR advection term and the subscript i symbolically indicates the spatial and angular grid points. Coefficients A, B, and C are written as a function of the space and flight directions. This fact suggests the following scheme for the advection term in SR:

$$F_{\rm adv} = F^{\rm SR}_{\rm adv}(f^n) + \left(F^{\rm NR}_{\rm adv}(f^{n+1}) - F^{\rm NR}_{\rm adv}(f^n)\right). \tag{30}$$

The first term on the right-hand side is the relativistic advection term evaluated with f^n and the second term in parentheses is a correction term. Equation (30) is only semi-implicit as is. Hence we replace f^n in Equation (30) with a trial value, $f^{\rm gs}$, and repeatedly solve the Boltzmann equation (Equation (27)), updating $f^{\rm gs}$ with f^{n+1} obtained for $f^{\rm gs}$ until they coincide with each other within a certain error. This ensures the full implicitness of our method as explained below.

The idea behind this method should be clear. If matter motion is not very fast compared with the speed of light, which is indeed the case in CCSNe, $F^{\rm SR}_{\rm adv}(f^{\rm gs})$ is almost equal to $F^{\rm NR}_{\rm adv}(f^{\rm gs})$, and $F_{\rm adv}$ will be dominated by $F^{\rm NR}_{\rm adv}(f^{n+1})$. Then this scheme is close to the NR implicit scheme. In addition, there are other important properties in the prescription: first, if $f^{\rm gs}$ coincides with f^{n+1}, as is the case at the end of iterations, the correction term vanishes and only $F^{\rm SR}_{\rm adv}(f^{\rm gs})(= F^{\rm SR}_{\rm adv}(f^{n+1}))$ remains. This property guarantees the full implicitness of our scheme. We also mention that Δt is actually limited most of time by the requirement that f should not change by more than a few percent in a single time step, and the correction term is a small correction to the first term in most situations (but see below for

[12] Note, however, that the collision terms can be easily treated implicitly. See the discussion at the end of this section.

the exceptional case.). In spite of this, we find that this correction term significantly improves the numerical stability, enabling us to take larger Δt.

Although the above method works fairly well most of the time, it fails sometimes when the matter velocity reaches several tens of percent of the speed of light and the correction term becomes significantly larger than $F^{\rm SR}_{\rm adv}(f^{\rm gs})$. In such cases, the iteration does not converge unless we reduce Δt. To avoid too small a value of Δt, however, we introduce a limiter, κ,

$$F_{\rm adv} = F^{\rm SR}_{\rm adv}(f^{\rm gs}) + \kappa\left(F^{\rm NR}_{\rm adv}(f^{n+1}) - F^{\rm NR}_{\rm adv}(f^{\rm gs})\right). \quad (31)$$

in which κ is determined so that the correction term does not exceed the first term. We stress that such a prescription is just a technique to improve the convergence and does not affect the final result since the second term vanishes in the end anyway.

We turn to the collision terms before closing this section. There are no new difficulties in their treatment since the LRG is essentially the same as the fluid restframe employed in the ordinary Lagrangian methods. There is one feature, however, which is original in our method. The angular dimensions in momentum space are discretized in the same manner everywhere on the LRG (see the left panel of Figure 4). This means that the angular gridding is not uniform in the fluid restframe due to an aberration caused by Lorentz transformation. The angular integration for the isoenergetic scattering, as shown in Equation (11), is normally performed in the fluid restframe. In our approach, however, this is done on the LRG in the laboratory frame. In so doing, the aberration effect is taken into account as the Jacobian in the following way:

$$\int A(\Omega^{\rm fr})d\Omega^{\rm fr} = \int B(\Omega^{\rm lb})\left(\frac{d\Omega^{\rm fr}}{d\Omega^{\rm lb}}\right)d\Omega^{\rm lb}, \quad (32)$$

where A is an arbitrary function of $\Omega^{\rm fr}$ and B is defined as $B(\Omega^{\rm lb}) \equiv A(\Omega^{\rm fr}(\Omega^{\rm lb}))$. The Jacobian $(d\Omega^{\rm fr}/d\Omega^{\rm lb})$ has already been derived in Equation (9).

As mentioned earlier, the collision terms are treated fully implicitly. The point is that the matrix structure originating from the collision terms is exactly the same as the one for the NR case, which implies that the numerical tools developed for our Newtonian code (Sumiyoshi & Yamada 2012) can be utilized for the present code as they are. As a matter of fact, thanks to this implicit treatment of collision terms, the time steps Δt in the 1D test simulation of CCSNe (see Section 7.5) are comparable to those in our previous simulations with a 1D implicit GR Lagrangian Boltzmann hydro code (Sumiyoshi et al. 2005).

6.5. Step 5: Feedback to Matter

Solving the Boltzmann equations in the previous step, we now treat feedback from the neutrino–matter interactions to hydrodynamics. The hydrodynamics equations and the equation for conservation of the number of electrons are written as[13]

$$T^{\mu\nu}_{{\rm hd},\nu} = -G^{\mu}, \quad (33)$$

$$N^{\nu}_{e,\nu} = -\Gamma, \quad (34)$$

where the right-hand sides correspond to the feedback and are written as

$$G^{\mu} \equiv \sum_i G^{\mu}_i, \quad (35)$$

$$G^{\mu}_i \equiv \int p^{\mu}_i \left(\frac{\delta f}{\delta \tau}\right)_{\rm col(i)} dV_p, \quad (36)$$

$$\Gamma \equiv \Gamma_{\nu_e} - \Gamma_{\bar{\nu}_e}, \quad (37)$$

$$\Gamma_i \equiv \int \left(\frac{\delta f}{\delta \tau}\right)_{\rm col(i)} dV_p. \quad (38)$$

In these expressions, the invariant volume in the momentum space is denoted by dV_p and the subscript "i" indicates the neutrino species.

At the very end of all of the steps, we again perform Steps 2 and 3 since matter velocities are changed due to the momentum exchange between matter and neutrinos. This closes the update from $t = t^n$ to $t = t^{n+1}$. We iterate these steps as many times as needed.

7. VALIDATION

In order to validate our new formulation of SR Boltzmann radiation hydrodynamics, we carry out a series of code tests. We first focus on the Boltzmann solver, i.e., the feedback to hydrodynamics is ignored. We test the advections and collisions separately in idealized setups in order to clearly see the code performance in each sector. In these tests, only electron-type neutrinos are taken into account since the treatments of SR effects are common to other species.

We then perform SR Boltzmann hydro simulations of 1D spherical core collapse for the 15 $M_\odot$ progenitor. In these test runs, we consider three species of neutrinos (ν_e, $\bar{\nu}_e$, and ν_x) and implement minimal but essential microphysics. For comparison, a NR simulation is also performed. Based on the two results, we discuss the importance of SR effects.

7.1. Collision Term: Isoenergetic Scattering

As discussed in Section 3, the isoenergetic scattering is the primary source of difficulties in the S_n method for the SR Boltzmann equation. This test is meant to see whether our code can properly handle this process. This is a single zone calculation, in which we deploy only one spatial grid and the advection term is neglected. We are concerned only with the collision term. Hydrodynamical quantities are assumed to be constant in time and set as $\rho = 10^{12}$ g cm^{-3}, $T = 2$ MeV, and $Y_e = 0.4$, where ρ, T, and Y_e denote the density, temperature, and electron fraction, respectively. Under this thermodynamical condition, both free nucleons and nuclei exist. Thus, we consider the following isoenergetic scatterings:

$$\nu + N \longleftrightarrow \nu + N \ , \quad (39)$$

$$\nu + A \longleftrightarrow \nu + A \ . \quad (40)$$

Although we drop the advection term in this test, we set a non-vanishing velocity as follows:

$$v^r = v\ \cos\theta_h, \quad (41)$$

$$v^{\theta} = v\ \sin\theta_h\ \cos\phi_h, \quad (42)$$

$$v^{\phi} = v\ \sin\theta_h\ \sin\phi_h, \quad (43)$$

[13] See Equations (12)–(16).

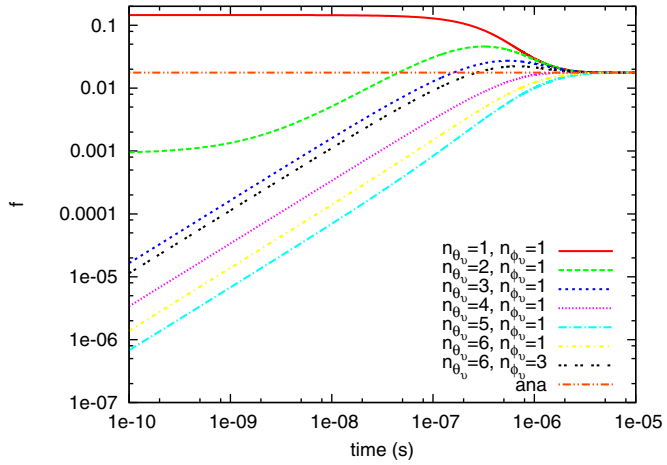

Figure 11. Time evolutions of f for different angles by the isoenergetic scatterings. n_{θ_υ} and n_{ϕ_υ} specify the angular grid points. The neutrino energy is set to 60 MeV in the fluid restframe. The orange dash-dotted line indicates the final state of f at $t \to \infty$ obtained analytically.

(A color version of this figure is available in the online journal.)

where v^r, v^θ, and v^ϕ denote the radial, θ, and ϕ components, respectively. They are assumed to be constant in time and are controlled by three parameters, v, θ_h and ϕ_h. In this test, we set $v = 2 \times 10^{10}$ cm s^{-1}, $\theta_h = \pi/4$, and $\phi_h = \pi/4$, respectively. Note that this velocity is considerably large by the CCSNe standard.

We assume that initially, neutrinos are distributed isotropically in the laboratory frame, and they have Fermi–Dirac distributions in energy. The neutrino chemical potential can be obtained by the assumption that neutrinos are in chemical equilibrium with matter. Since matter has a non-vanishing velocity, neutrinos are initially *anisotropic* in the fluid restframe. Then, f should evolve toward an isotropic distribution in the latter frame due to isoenergetic scattering.

For this test, momentum space is covered with a grid of $N_\epsilon(= 20)$ points in energy and $N_{\theta_\upsilon}(= 6) \times N_{\phi_\upsilon}(= 6)$ points in angles. The gridding of the LRG has been explained in detail in Section 5 and Figure 4 (see also Sumiyoshi & Yamada 2012 for the construction of angular grid).

We show the numerical results in Figures 11–15. Figure 11 displays the evolutions of f for different angles but with the same energy ($\varepsilon^{\rm fr} = 60$ MeV) in the fluid restframe. As is expected, initially different values of f are changed by the isoenergetic scatterings and converge to a certain value by the time $t \sim 10^{-5}$ s. Note that we work on the LRG in the laboratory frame and these results are obtained by the Lorentz transformation to the fluid restframe. The final isotropic distribution, $f_{\rm iso}$, can be obtained analytically from the initial condition, $f_{\rm ini}$, since isoenergetic scatterings do not change the number of neutrinos:

$$f_{\rm iso}(\varepsilon^{\rm fr}) = \frac{\sum_i f_{\rm ini}(\varepsilon^{\rm lb}(\varepsilon^{\rm fr}), \Omega^{{\rm lb}(i)})(D^{{\rm lb}(i)})^{-3}(\Delta\Omega^{{\rm lb}(i)})}{\sum_{\rm i}(D^{{\rm lb}(i)})^{-3}(\Delta\Omega^{{\rm lb}(i)})}, \quad (44)$$

where the subscript i specifies the angular grid points. It is evident from the figure that the correct results are obtained numerically.

Figure 12 shows the angular evolution of f on an isoenergy surface with $\varepsilon^{\rm fr} = 60$ MeV in the fluid restframe. In the figure, wire-framed pictures are drawn as follows: for each angular grid point, a node is placed at a distance proportional to the value of f in the corresponding direction, the neighboring nodes are then connected by lines, and we use the normalization in which the maximum distance should be unity. As a consequence, an isotropic distribution corresponds to the unit sphere in this figure.

At the beginning (top left panel), the wire frame is elongated in one direction, indicating that the angular distribution is highly anisotropic. As time passes, however, it changes shapes and eventually ($t \sim 10^{-5}$ s) becomes isotropic although it may

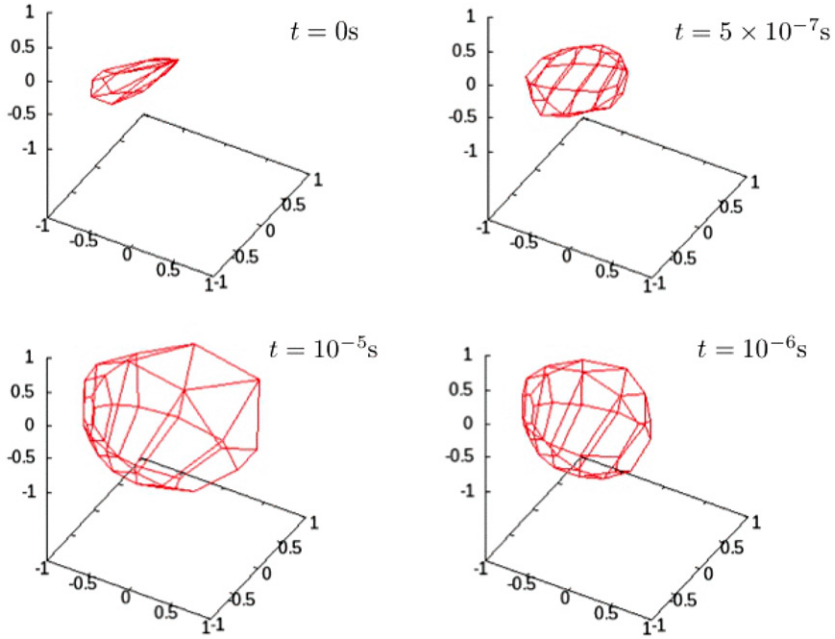

Figure 12. 3D presentations of f in the fluid restframe at different times. Only the angular distributions are shown for neutrinos with an energy of 60 MeV in the fluid restframe. See the text for more details on the construction of wire frames.

(A color version of this figure is available in the online journal.)

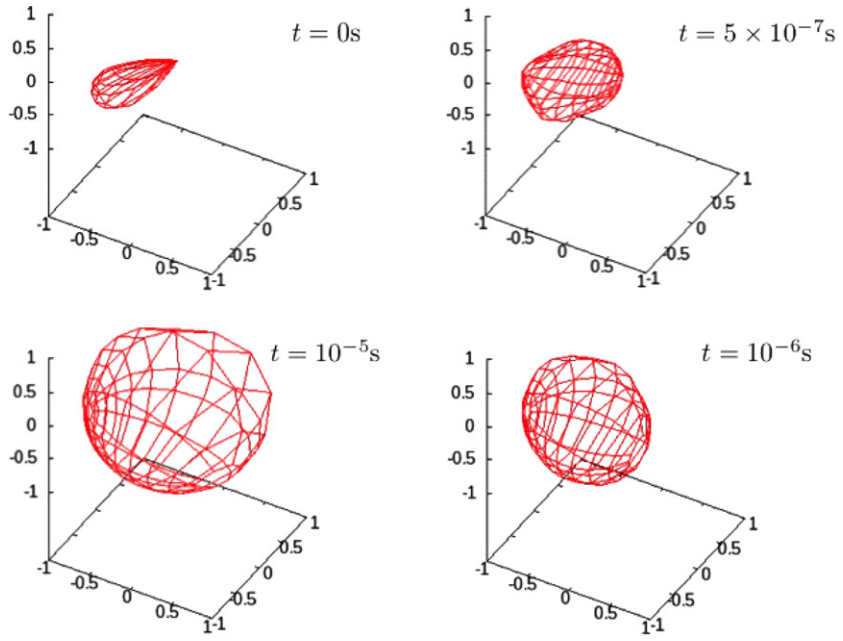

Figure 13. Same as Figure 12 but for a higher angular resolution ($N_{\theta_\nu} = 12$, $N_{\phi_\nu} = 12$).
(A color version of this figure is available in the online journal.)

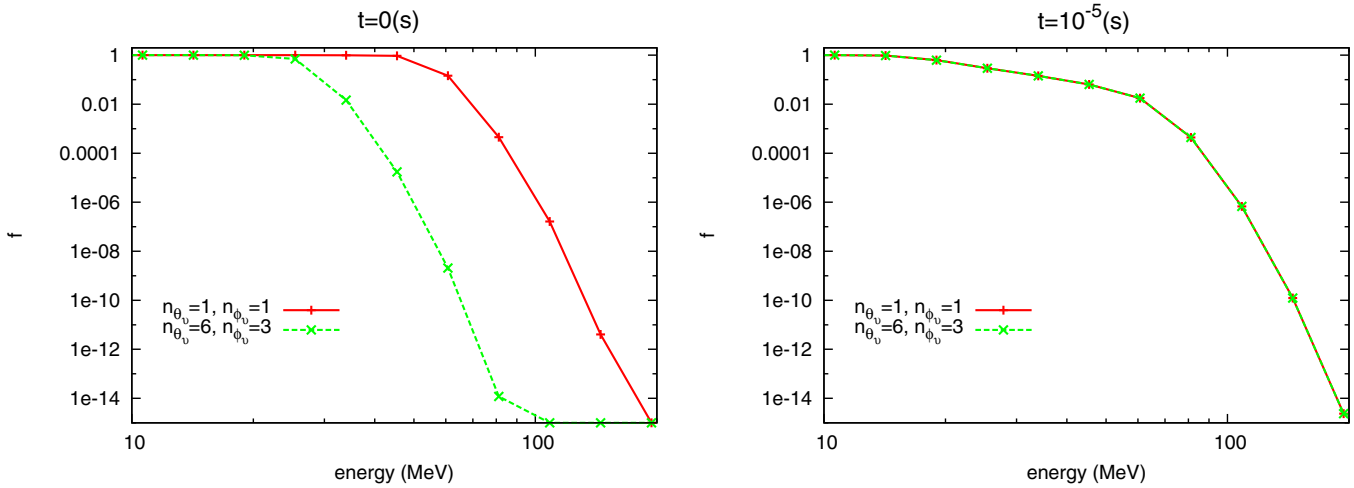

Figure 14. Energy spectra for different flight directions in the fluid restframe at two different times (left: $t = 0$ s, right: $t = 10^{-5}$ s). Note that the floor value of f is set as 10^{-15}, which is observed at high energies.
(A color version of this figure is available in the online journal.)

not appear so. This is due to the rather low resolution in this computation. Indeed, Figure 13, which presents the result for a higher resolution ($N_{\theta_\nu} = 12$, $N_{\phi_\nu} = 12$) more clearly isotropic of the final distribution. We also remind the reader that the angular grid is not uniform in the fluid restframe due to an aberration (it is uniform in the laboratory frame; see Section 5).

As an alternative presentation of isotropy, in Figure 14 we show the initial and final energy spectra for two different angles in the fluid restframe. As demonstrated clearly in this figure, the initially different spectra converge at the end, implying that neutrino distributions become isotropic at all energies. In Figure 15 we show the same evolution in the laboratory frame, which is actually the frame we use for simulations. Contrary to the previous case, the initially identical spectrum for different angles is separated as time passes in the laboratory frame, indicating that the final distribution is anisotropic in this frame as it should be.

7.2. Collision Term: Emission, Absorption, and Isoenergetic Scattering Combined

To the isoenergetic scatterings, we add emissions and absorptions on nucleons and nuclei:

$$e^- + p \longleftrightarrow \nu_e + n, \tag{45}$$

$$e^+ + n \longleftrightarrow \bar{\nu}_e + p, \tag{46}$$

$$e^- + A \longleftrightarrow \nu_e + A'. \tag{47}$$

The initial condition and computational setup are the same as those in the previous test.

Figure 16 shows the evolution of f for different angles but with the same energy ($\varepsilon^{\rm fr} = 60$ MeV) in the fluid restframe, which corresponds to Figure 11. At first, the isoenergetic scatterings cause the distribution in the fluid restframe to reach

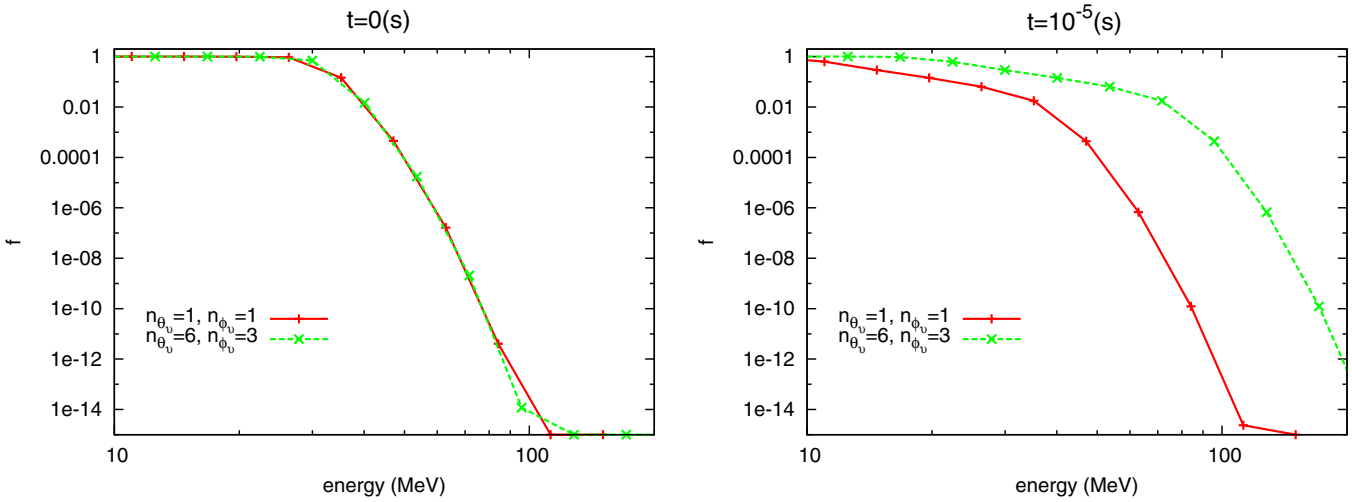

Figure 15. Same as Figure 14 but in the laboratory frame.
(A color version of this figure is available in the online journal.)

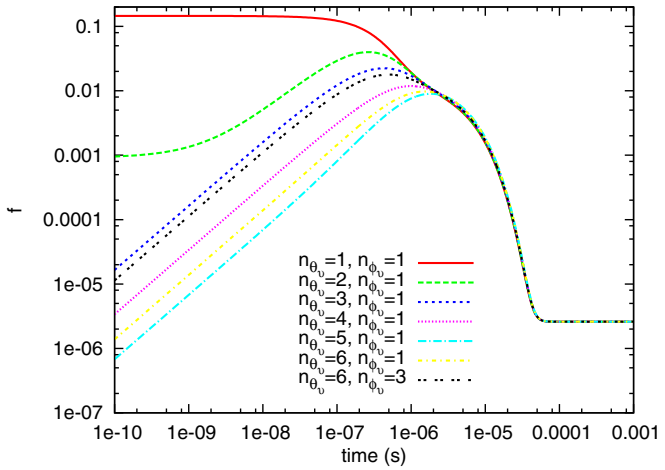

Figure 16. Same as Figure 11 but including emission and absorption processes.
(A color version of this figure is available in the online journal.)

isotropy as in the previous case. By the time $t \sim 10^{-5}$ s, the neutrino distribution is almost isotropic. Note that this is not a Fermi–Dirac distribution, i.e., neutrinos have not yet achieved chemical equilibrium with matter via emissions and absorptions. Equilibrium is eventually established at $t \sim 10^{-4}$ s for this level of energy for neutrinos. Neutrinos with other levels of energy undergo similar evolutions and reach Fermi–Dirac distributions at different times. We stress again that this computation is done on the LRG and the distribution in the fluid restframe is obtained via a Lorentz transformation.

7.3. Advection Term: 1D Advection through a Discontinuity in Matter

We now turn to the advection term. Note that this is the main source of difficulty in using the ordinary Lagrangian methods. Our formulation treats the spatial and angular advections in the laboratory frame but employs interpolations between two grids (LRG and LFG) as detailed in Section 6.4. It is hence important to confirm that the scheme indeed works properly.

Here, we consider the advection in matter that has a discontinuous velocity distribution. This is certainly the most difficult situation for our method. In contrast to the previous tests, we cut off all neutrino–matter reactions, assuming that the matter is optically thin, and consider the advection term alone. Note that in this case, the energy spectrum of neutrinos is unchanged as they propagate through the discontinuity in the laboratory frame whereas it undergoes a discontinuous change there in the fluid restframe (see also Figure 5). We further assume spherical symmetry in this test, i.e., we omit derivative terms with respect to θ, ϕ, and ϕ_ν in Equation (2).

The computational setup is as follows. To avoid geometrical complications, we consider the advection in a wafer-thin spherical shell: the computational domain covers the range of $10^8 < r < (10^8 + 10^5)$ cm by a uniform radial grid of six bins. The matter velocity is piecewise constant with a discontinuity between the third and fourth grid points: $v = 0$ for the first three grid points and $v = -2 \times 10^{10}\,\mathrm{cm\,s^{-1}}$ for the rest of the grid points. These velocities are again fixed during the computation. We inject outgoing neutrinos from the radial inner boundary with the Fermi–Dirac distribution, which is the same as in the previous tests, and we follow the subsequent evolution until a steady state is obtained. We deploy an LRG of $N_\epsilon = 20$ and $N_{\theta_\nu} = 6$.

Figure 17 shows that the energy spectra for outgoing neutrinos ($n_{\theta_\nu} = 6$) in the vicinity of the velocity discontinuity in the laboratory frame (left panel) and in the fluid restframe (right panel). As is expected, neutrinos advect without any change of their spectrum when they pass through the discontinuity in the laboratory frame. We can also see in this figure that the energy bins for the outer two radial grid points are shifted from those for the inner two. The right panel shows the same spectrum but observed in the fluid restframe. Due to the negative radial velocity in the outer region, neutrinos are blueshifted there (see also Figure 5). As demonstrated clearly in this test, our new formulation can reproduce the results just as expected without any numerical problems.

7.4. Advection Term: 3D Advection

This test is meant to check the multi-D advection in the optically thin matter with an inhomogeneous non-radial velocity distribution. We assume that the neutrino distribution is spherically symmetric in space. This is no problem, since the matter is optically thin and there is no interaction between the matter and neutrinos. This poses a challenge in our method, however, since the LRG is not spherically symmetric in space and, as a consequence, there is no guarantee that the neutrino distribution

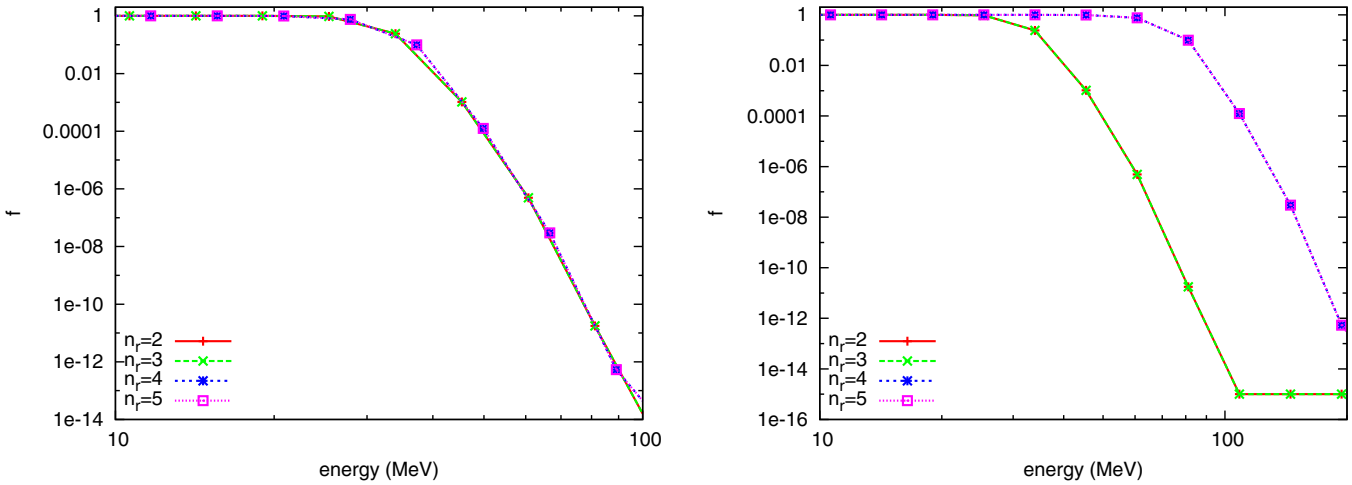

Figure 17. Energy spectra of outgoing neutrinos at different radii in the vicinity of the discontinuity in the laboratory frame (left) and in the fluid restframe (right). n_r specifies the radial grid point. Note that the floor value of f is set to be 10^{-15}.
(A color version of this figure is available in the online journal.)

remains spherically symmetric in our formulation. This test is hence a good diagnostic of our handling of the spatial advection.

The 3D velocity distribution is set in a similar way to that in the previous test, Equation (43), but with an additional spatial dependence:

$$v^r(r,\theta,\phi) = v(r,\theta,\phi)\ \cos\theta_h, \tag{48}$$

$$v^\theta(r,\theta,\phi) = v(r,\theta,\phi)\ \sin\theta_h\ \cos\phi_h, \tag{49}$$

$$v^\phi(r,\theta,\phi) = v(r,\theta,\phi)\ \sin\theta_h\ \sin\phi_h. \tag{50}$$

We again set a non-vanishing non-radial velocity by choosing $\theta_h = \pi/4$, and $\phi_h = \pi/4$. $v(r,\theta,\phi)$ is given as follows:

$$\begin{aligned} v(r,\theta,\phi) &= 2\times 10^{10}\cos A_r(r) \\ &\quad \times \cos\theta\ \cos\phi \qquad (\mathrm{cm\,s^{-1}}), \\ A_r(r) &= 2\pi\times\frac{r-r_{\rm min}}{r_{\rm max}-r_{\rm min}}, \end{aligned} \tag{51}$$

where $r_{\rm max}$ and $r_{\rm min}$ denote, respectively, the maximum and minimum radii of the computational region, which is the spherical shell with $r_{\rm min} = 10^8 < r < r_{\rm max} = 10^8 + 10^9$ cm, $0 < \theta < \pi$ and $0 < \phi < 2\pi$. We deploy to this computational domain an LRG with $N_r = 6, N_\theta = 4, N_\phi = 6, N_\epsilon = 20, N_{\theta_\nu} = 6, N_{\phi_\nu} = 6$. In the following, we demonstrate that the neutrino distribution remains spherically symmetric with this small number of spatial and angular grid points. We inject from the inner boundary outgoing neutrinos with the same Fermi–Dirac distribution employed in the previous tests. The simulation is continued until the neutrino distribution becomes steady.

We summarily display the results of this test in Figure 18. The upper left panel shows the energy spectra for different n_{ϕ_ν}'s (with $n_{\theta_\nu} = 6$ being fixed) at $n_r = 6$ and $n_\theta = 1$ in the laboratory frame. Note that if the neutrino distribution is exactly spherically symmetric, these spectra should coincide with each other. As seen in this figure, they agree quite well despite the fact that they are computed on the LRG, which is not spherically symmetric. The upper right panel is the same as the upper left, but for $n_{\theta_\nu} = 4$. Note that these neutrinos propagate in a non-radial direction. Again their spectra depend on ϕ_ν very weakly. Finally, in the bottom panel we display the energy spectra at a different radial location $n_r = 6$. This time, $n_{\theta_\nu} = 6$ and $n_{\phi_\nu} = 1$ are fixed and n_θ is varied. We can also confirm in this case that all energy spectra are in good agreement. It is emphasized again that these results are not trivial and, in fact, the test is very severe, since we assume here very fast matter motions (∼60% of the speed of light) with large inhomogeneities. We thus think that our new method works satisfactorily.

7.5. SR Boltzmann Hydro Simulations: The Spherical Collapse of 15 $M_\odot$ Progenitor

So far we have tested the advection and collision separately in simplified setups. In reality, however, they are non-linearly coupled with each other and dictate the neutrino transfer and, as a consequence, the dynamics of CCSNe. In order to confirm that our new method is indeed applicable to realistic simulations of CCSNe, we conduct here a 1D spherically symmetric Boltzmann hydro simulation for the collapse of 15 $M_\odot$ progenitor (a non-rotating star with the solar metallicity referred to as s15.0 in Woosley et al. 2002). We employ an LRG with $N_r = 300, N_\epsilon = 20, N_{\theta_\nu} = 8$ covering the computational domain of $0 < r < 4\times10^8$ cm. For comparison, we also perform an NR simulation for the same setup. Although the simulation is continued after bounce until the shock wave is stalled, we focus here on the collapsing phase, since the infall velocity is largest and SR effects are most clearly discernible.

Figure 19 shows that the evolution of the number density of ν_e at the center for both the SR and NR simulations. Initially these two simulations follow almost the same evolutionary path. After the central density reaches $\rho_c \sim 10^{12}$ g cm^{-3}, however, they start to deviate and become different by more than a factor of ∼4 at $\rho_c \sim 10^{14}$ g cm^{-3}. During the latter period, neutrinos undergo isoenergetic scatterings on nuclei called coherent scatterings and, as shown, this is in fact the source of the discrepancy.

In order to clearly see the SR effects from the matter motion, the left panels of Figure 20 show the radial component of the amount of flux, i.e., the energy-integrated first-angular moment of f_{ν_e} in the laboratory frame, as a function of radius:

$$F^r(r) \equiv \int \cos\theta_\nu\, f(r,\Omega^{\rm lb},\varepsilon^{\rm lb}) d\Omega^{\rm lb} dV_\varepsilon^{\rm lb}, \tag{52}$$

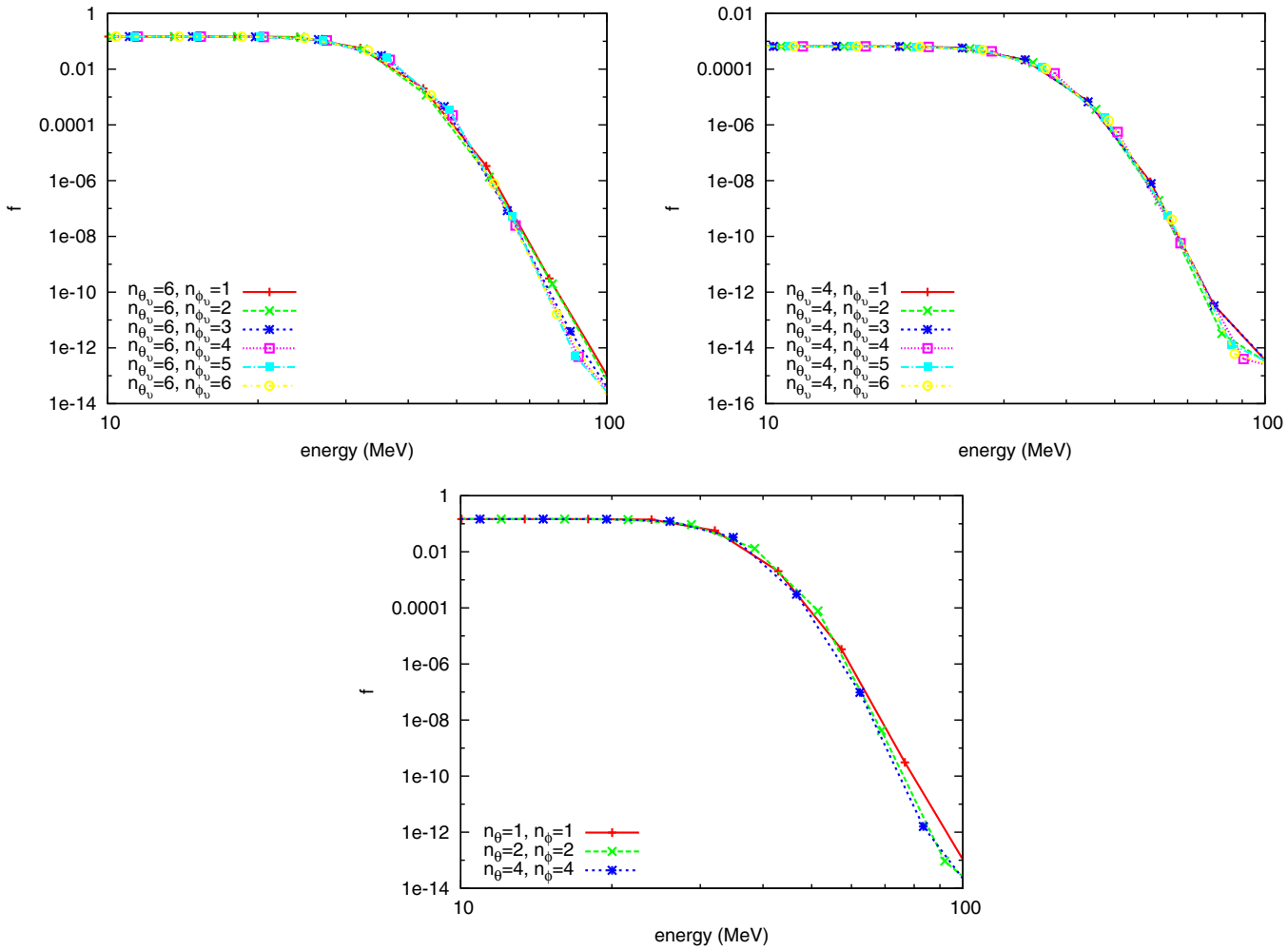

Figure 18. Energy spectra at different points in phase space. Upper left: $n_r = 6$, $n_\theta = 1$, $n_{\theta_\upsilon} = 6$ and different n_{ϕ_υ}. Upper right: the same as the upper left but for $n_{\theta_\upsilon} = 4$. Bottom panel: the same as the previous two panels but for $n_r = 6$, $n_{\theta_\upsilon} = 6$, and $n_{\phi_\upsilon} = 1$.

(A color version of this figure is available in the online journal.)

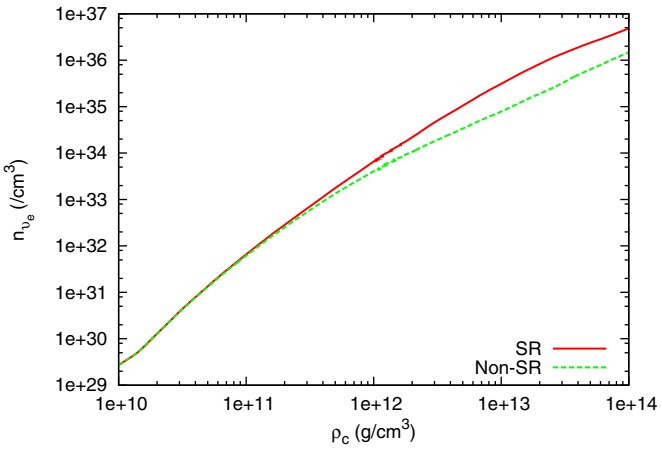

Figure 19. Evolution of the number density of electron-type neutrinos at the center in both the SR (red solid line) and NR (green dashed line) simulations. The central matter density instead of the time is used to parameterize the evolutions.

(A color version of this figure is available in the online journal.)

where $dV_\varepsilon^{\rm lb}$ denotes the volume element of energy space in the laboratory frame. The upper panel corresponds to the time when the central density reaches $\rho_c = 10^{12}\,{\rm g\,cm^{-3}}$ whereas the bottom one shows the result at the time of $\rho_c = 10^{14}\,{\rm g\,cm^{-3}}$, respectively. On the right panels, matter velocities are displayed as a function of time.

As is evident in the left panels, the amount of flux behaves qualitatively differently in the SR and NR cases: F^r in the SR simulation is negative in the inner region ($r \lesssim 60$ km), whereas it is positive everywhere in the NR. Simply put, neutrinos are moving in the opposite direction if SR is ignored. This is understood as follows (see also Section 2). Matter is optically thick to neutrinos in the inner region and neutrinos tend to diffuse outward as observed in the NR simulation. On the other hand, the matter is infalling and tends to drag neutrinos inward; this is made possible by frequent interactions between the matter and neutrinos. In fact, as demonstrated in Sections 7.1 and 7.2, scatterings and emissions/absorptions render the neutrino distribution isotropic in the fluid restframe and, as a consequence, produce a flux in the direction of the velocity in the laboratory frame after Lorentz transformation; if SR is neglected, neutrinos are isotropically distributed even in the laboratory frame and no dragging occurs; this is the cause for the discrepancy. Note that this dragging (and hence SR) is crucially important for neutrino trapping as shown next.

In Figure 21, we display the radial distribution of the lepton fraction at two different times: when the central density reaches $\rho_c = 10^{13}$ and $10^{14}\,{\rm g\,cm^{-3}}$. The left panel presents the results of the SR simulation, while the right panel gives the

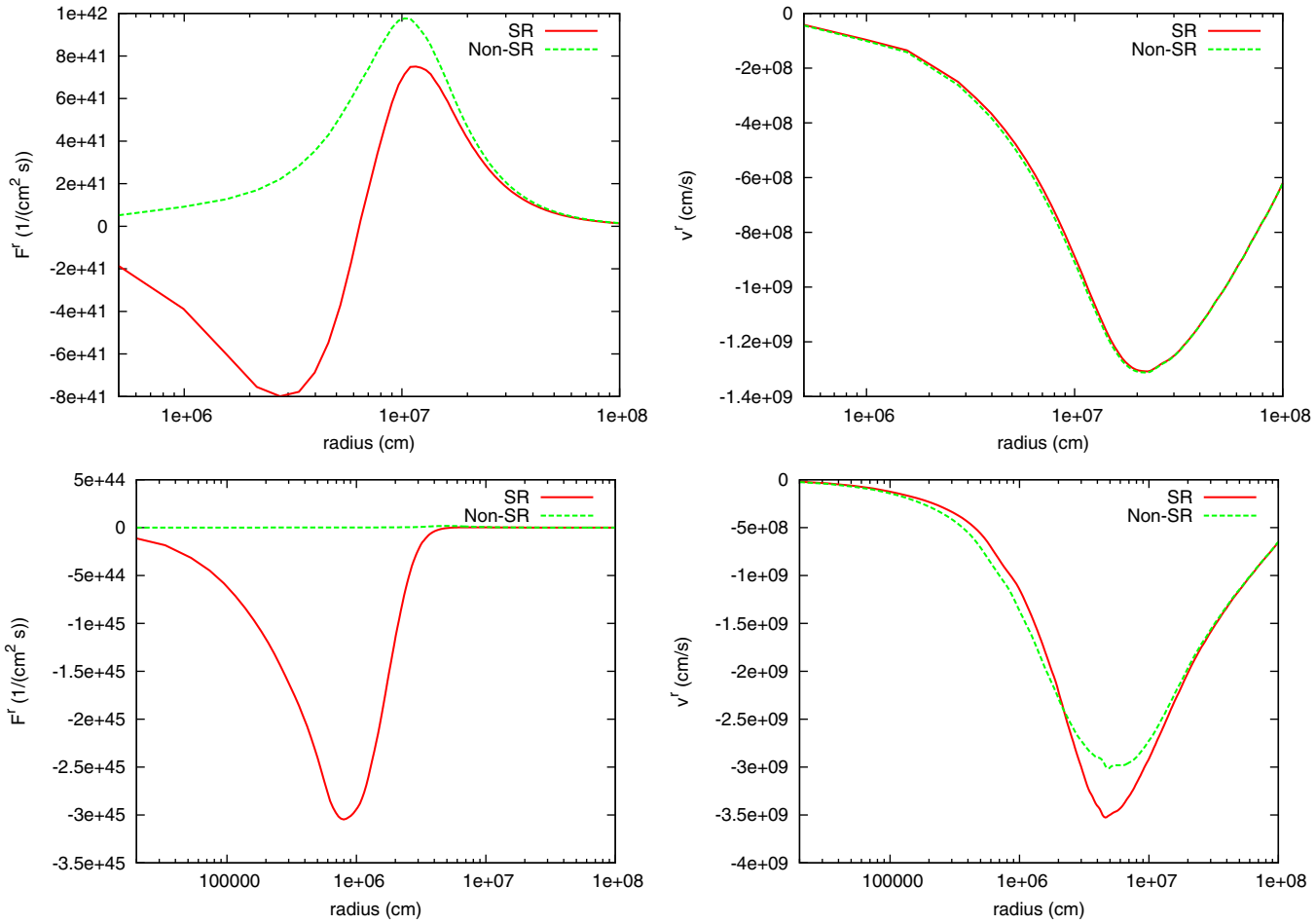

Figure 20. Radial distributions of the radial ν_e number flux in the laboratory frame (left panels) and those of the radial matter velocity (right panels). Upper panels show the results at the time when the central density ρ_c reaches $10^{12}\,\mathrm{g\,cm^{-3}}$, whereas lower panels correspond to the time of $\rho_c = 10^{14}\,\mathrm{g\,cm^{-3}}$. The red (green) lines are obtained in the SR (NR) simulations.

(A color version of this figure is available in the online journal.)

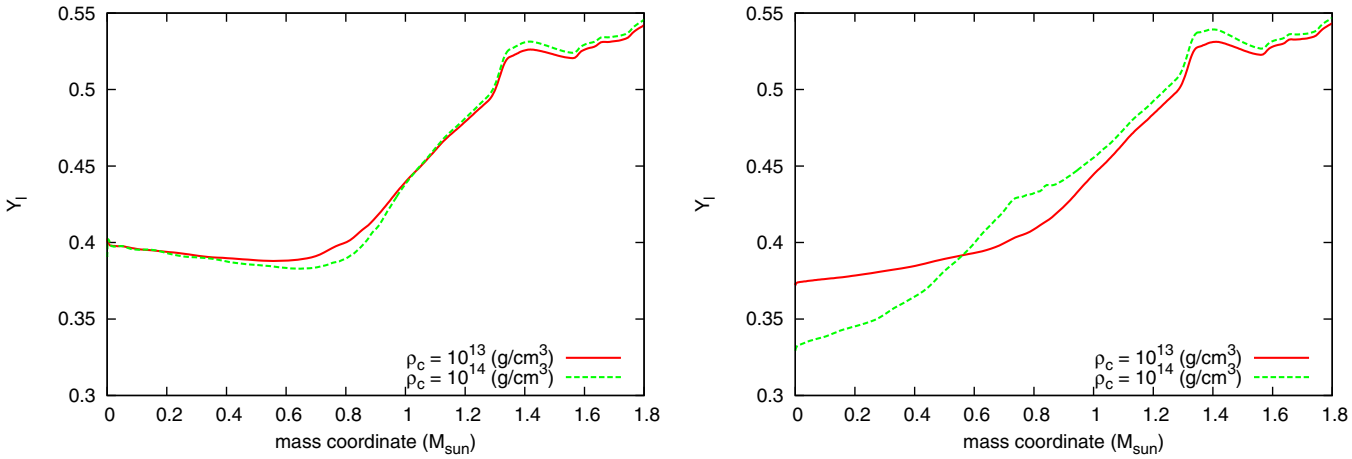

Figure 21. Distributions of Y_l at two different times. The red (green) lines correspond to the time when the central density reaches $\rho_c = 10^{13}(10^{14})\,\mathrm{g\,cm^{-3}}$. The left panel shows the result in the SR simulation and the right panel is the NR counterpart.

(A color version of this figure is available in the online journal.)

NR counterpart. We can immediately recognize a remarkable difference. In the SR simulation, two lines are almost the same, in particular for $M_r < 0.6\,M_\odot$, where M_r denotes the mass coordinate. This means that the lepton number is conserved in each fluid element as it should be after neutrino trapping. For the NR case, on the other hand, the lepton fraction is decreased even in the central region while it is increased in the outer region. This means that neutrinos are diffusing outward in the Lagrangian frame even after neutrino trapping, which is consistent with what we observed in the number flux above.

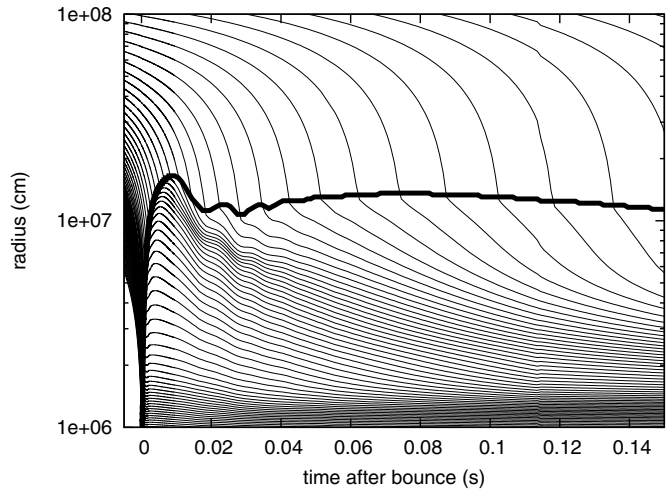

Figure 22. Mass shell trajectories in the post-bounce phase. The thick line shows the trajectory of shock wave.

In the Lagrangian method, the lepton number conservation after neutrino trapping is handled almost trivially. Our Boltzmann hydro solver is based on the Eulerian picture, in which Y_l evolves as a function of radius even after neutrino trapping. Only when SR is taken into account appropriately can we reproduce the correct evolutions. The results of this test simulation are hence the clearest evidence that our new method properly handles neutrino advection. Incidentally, we have also made a comparison with the result of 1D Lagrangian GR simulations (Sumiyoshi et al. 2005)[14] and confirmed reasonable agreement between them (although not shown here).

Finally, we present the mass shell trajectories during the post-bounce phase (until 150 ms after the bounce) in Figure 22. After bounce, the shock wave propagates outward initially through optically thick matter and generates a neutronization burst of ν_e when it breaks out of the neutrino sphere and is eventually stagnated at a certain radius in optically thin matter. These phases are, in general, numerically difficult for our method since neutrino distributions evolve quite rapidly, both optically thick and thin regions are involved, and a shock wave, i.e., a discontinuity in matter velocities, exists. In spite of these difficulties, our SR Boltzmann hydro code has run stably without problems. Although we have to wait for more detailed quantitative analyses of this model and others in multi-D, which will be reported elsewhere as a follow-up to this paper, the results shown so far indicate that our new code will be applicable to realistic CCSNe simulations.

8. SUMMARY AND POSSIBLE EXTENSIONS OF THE FORMULATION

In this paper, we have presented a novel method for numerically solving the SR Boltzmann equation in the laboratory frame based on the S_n method, which overcomes technical difficulties inherent in the conventional approaches irrespective of the Lagrangian or Eulerian pictures. Our method is hybrid, deploying LRGs in the laboratory frame. The employment of the LRG simply solves the difficulties in the treatment of scattering, which plagues the conventional Eulerian approaches. As a trade-off, the numerical treatment of the advection term becomes complicated as in the ordinary Lagrangian approaches. This problem is mitigated by the use of the LFG, which is nothing but the ordinary grid fixed to the laboratory frame and adopted in the conventional Eulerian approaches. The advection becomes simplest on the LFG. We have developed a scheme for the interpolation between the LRG and LFG, which ensures that the number of neutrinos is conserved.

By carrying out a series of code tests, we have demonstrated that our new method works as expected, correctly handling both the collision and advection terms. With the same code, we have also conducted 1D CCSNe simulations from core collapse through bounce until shock stall for a realistic progenitor model of $15\,M_\odot$ with the minimal set of microphysics. We have paid particular attention to the collapsing phase, in which matter velocities reach maximum and our code faces the greatest challenge. We have found that the neutrino dragging due to matter motions, which is crucially important in neutrino trapping, is correctly captured in the SR simulation but not in the NR one. We have also observed only in the SR computation that the lepton fraction as a function of the Lagrangian mass coordinates does not change with time in the optically thick region. These results clearly indicate that the adequate treatment of SR effects is critically important to correctly obtain the lepton fraction.

The simulation was continued until the shock wave generated at bounce was stalled in the core. We have found no problem in the later phase, either, and we are now confident that our new method is applicable to the realistic simulation of CCSNe. In fact, we have already started such simulations in 2D and their results will be reported, together with further tests in multi-D, in our forthcoming paper. We finally stress that our method could be applied to other more relativistic phenomena such as photon transfer in active galactic nuclei or gamma-ray bursts, since SR effects are taken into account to all orders of v/c in our Boltzmann code. These possibilities will be studied in the future.

We have also commented on the extension of our formulation to GR Boltzmann hydro simulations. We have recently published a paper on the conservative form of the GR Boltzmann equation (Shibata et al. 2014), which, in flat spacetime, would reduce to the one used in the current study. It turns out that our Lagrangian remapping method can be extended to this form of GR Boltzmann equation with some modifications. As shown in Equation (21) of that paper, GR modifies only the advection terms with the collision terms being essentially unchanged from the SR case. In the GR case, the choice of LFG is nontrivial. We may be able to use a local tetrad with a time-like unit vector, n^a, orthogonal to the spatial hypersurface of $t = \text{const}$. Then one important difference from the SR case is that n^a depends on space and time, which implies that the GR Boltzmann equation has energy-derivative terms on the left-hand side even in the laboratory frame, which is nothing but gravitational redshift. We note, however, that these terms may not pose problems since the gravitational field changes only gradually both in time and space. Such an extension is currently underway and will be published elsewhere.

We are grateful to Y. Sekiguchi, A. Mezzacappa, W. Iwakami, and S. Furusawa for valuable comments on the multi-D neutrino transfer simulations. We also thank A. Imakura, T. Sakurai, and H. Matsufuru for the development of the matrix solver for the Boltzmann equation. The numerical computations were partially performed on the supercomputers at the High Energy Accelerator Research Organization (KEK) under the

[14] In the comparison, we turn off the electron scattering in the Lagrangian GR simulation. Note that the GR effect is negligible for Y_l before bounce.

support of its Large Scale Simulation Program (13/14-10). We acknowledge the supercomputing resources at Yukawa Institute for Theoretical Physics (YITP) at Kyoto University. This work was supported by a Grant-in-Aid for Scientific Research from the Ministry of Education, Culture, Sports, Science, and Technology (MEXT) of Japan (22540296, 24103006, 24740165, and 24244036) and the HPCI Strategic Program of the Japanese MEXT and the K computer at the RIKEN (Project ID: hpci 130025, 140211).

REFERENCES

Burrows, A. 2013, RvMP, 85, 245
Burrows, A., Dessart, L., & Livne, E. 2007, in AIP Conf. Proc. 937, Supernova 1987A: 20 Years After: Supernovae and Gamma-Ray Bursters, ed. A. Burrows, L. Dessart, & E. Livne (Melville, NY: AIP), 370
Burrows, A., Livne, E., Dessart, L., Ott, C. D., & Murphy, J. 2006, ApJ, 640, 878
Cardall, C. Y., Endeve, E., & Mezzacappa, A. 2013, PhRvD, 88, 023011
Cardall, C. Y., Lentz, E. J., & Mezzacappa, A. 2005, PhRvD, 72, 043007
Dolence, J. C., Burrows, A., Murphy, J. W., & Nordhaus, J. 2013, ApJ, 765, 110
Hubeny, I., & Burrows, A. 2007, ApJ, 659, 1458
Janka, H.-T. 2012, ARNPS, 62, 407
Kitaura, F. S., Janka, H.-T., & Hillebrandt, W. 2006, A&A, 450, 345
Kotake, K., Sumiyoshi, K., Yamada, S., et al. 2012a, arXiv:1205.6284
Kotake, K., Takiwaki, T., Suwa, Y., et al. 2012b, PTEP, 2012, 010000
Kurganov, A., & Tadmor, E. 2000, JCoPh, 160, 241
Lentz, E., Bruenn, S. W., Harris, J. A., et al. 2012, in Proc. of the XII International Symposium on Nuclei in the Cosmos (NIC XII), http://pos.sissa.it/cgi-bin/reader/conf.cgi?confid=146, id. 208
Liebendörfer, M., Rampp, M., Janka, H.-T., & Mezzacappa, A. 2005, ApJ, 620, 840
Marek, A., & Janka, H.-T. 2009, ApJ, 694, 664
Mezzacappa, A., & Bruenn, S. W. 1993, ApJ, 405, 669
Mezzacappa, A., Liebendörfer, M., Messer, O. E., et al. 2001, PhRvL, 86, 1935
Müller, B., Janka, H.-T., & Dimmelmeier, H. 2010, ApJS, 189, 104
Müller, B., Janka, H.-T., & Heger, A. 2012a, ApJ, 761, 72
Müller, B., Janka, H.-T., & Marek, A. 2012b, ApJ, 756, 84
Nagakura, H., Ito, H., Kiuchi, K., & Yamada, S. 2011, ApJ, 731, 80
Nagakura, H., & Yamada, S. 2008, ApJ, 689, 391
Nagakura, H., Yamamoto, Y., & Yamada, S. 2013, ApJ, 765, 123
Ott, C. D., Burrows, A., Dessart, L., & Livne, E. 2008, ApJ, 685, 1069
Peres, B., Penner, A. J., Novak, J., & Bonazzola, S. 2014, CQGra, 31, 045012
Shen, H., Toki, H., Oyamatsu, K., & Sumiyoshi, K. 2011, ApJS, 197, 20
Shibata, M., Nagakura, H., Sekiguchi, Y., & Yamada, S. 2014, PhRvD, 89, 084073
Sumiyoshi, K., Takiwaki, T., Matsufuru, H., & Yamada, S. 2014, arXiv:1403.4476
Sumiyoshi, K., & Yamada, S. 2012, ApJS, 199, 17
Sumiyoshi, K., Yamada, S., & Suzuki, H. 2007, ApJ, 667, 382
Sumiyoshi, K., Yamada, S., Suzuki, H., et al. 2005, ApJ, 629, 922
Suwa, Y., Kotake, K., Takiwaki, T., et al. 2010, PASJ, 62, L49
Takiwaki, T., Kotake, K., & Suwa, Y. 2012, ApJ, 749, 98
Takiwaki, T., Kotake, K., & Suwa, Y. 2014, ApJ, 786, 83
Woosley, S. E., Heger, A., & Weaver, T. A. 2002, RvMP, 74, 1015